NPS 69Ps-78-002

NAVAL POSTGRADUATE SCHOOL

Monterey, California

CORROSION BEHAVIOR OF ALUMINUM ALLOYS INTENDED FOR SACRIFICIAL ANODE APPLICATION IN SEAWATER

J. Perkins, J. R. Cummings,
R. A. Reinhardt, and K. J. Graham

March 1978

Technical Report No. 6
To the Office of Naval Research
Contract No. N00014-78-WR-80105
NR 036-120

NAVAL POSTGRADUATE SCHOOL
Monterey, California

Rear Admiral T. R. Dedman
Superintendent

Jack R. Borsting
Provost

The work reported herein was supported by the Office of Naval Research, Naval Ship Systems Command, Metallurgy Program Office, Code 471, Arlington, VA, 22217, through Contract No. N00014-78-WR-80105, NR-036-120.

This report was prepared by:

UNCLASSIFIED

SECURITY CLASSIFICATION OF THIS PAGE *(When Data Entered)*

REPORT DOCUMENTATION PAGE

READ INSTRUCTIONS BEFORE COMPLETING FORM

1. REPORT NUMBER: NPS-69Ps-78-002	2. GOVT ACCESSION NO.
3. RECIPIENT'S CATALOG NUMBER	
4. TITLE *(and Subtitle)*: CORROSION BEHAVIOR OF ALUMINUM ALLOYS INTENDED FOR SACRIFICIAL ANODE APPLICATION IN SEAWATER	
5. TYPE OF REPORT & PERIOD COVERED: Interim, 10/77 to 3/78	
6. PERFORMING ORG. REPORT NUMBER: Technical Report No. 6	
7. AUTHOR(s): Jeff Perkins, J. R. Cummings, R. A. Reinhardt, and K. J. Graham	
8. CONTRACT OR GRANT NUMBER(s): N00014-78-WR-80105, NR-036-120	
9. PERFORMING ORGANIZATION NAME AND ADDRESS: Materials Science and Chemistry Group, Code 69Ps Department of Mechanical Engineering, Naval Postgraduate School, Monterey, CA 93940	
10. PROGRAM ELEMENT, PROJECT, TASK AREA & WORK UNIT NUMBERS: Program Element: 61153N Project: RR022-08-01	
11. CONTROLLING OFFICE NAME AND ADDRESS: Office of Naval Research, Metallurgy Program Office, Code 471, Arlington, VA 22217	
12. REPORT DATE: March 1978	
13. NUMBER OF PAGES	
14. MONITORING AGENCY NAME & ADDRESS *(if different from Controlling Office)*	
15. SECURITY CLASS. *(of this report)*: UNCLASSIFIED	
15a. DECLASSIFICATION/DOWNGRADING SCHEDULE	

16. DISTRIBUTION STATEMENT *(of this Report)*

Approved for public release; distribution unlimited.
Reproduction in whole or in part is permitted for any purpose of the United States Government.

17. DISTRIBUTION STATEMENT *(of the abstract entered in Block 20, if different from Report)*

18. SUPPLEMENTARY NOTES

19. KEY WORDS *(Continue on reverse side if necessary and identify by block number)*

aluminum anodes, cathodic protection, sacrificial anodes, pitting, dissolution

20. ABSTRACT *(Continue on reverse side if necessary and identify by block number)*

The corrosion behavior of several commercial aluminum sacrificial anode alloys were studied. Laboratory-scale experiments were conducted to establish the galvanic current output characteristics of the alloys when coupled to HY-80 steel in synthetic seawater. Also direct weight loss measurements of corrosion rates and potentiostatic polarization behavior were obtained, and the mode and distribution of corrosive attack on the various anode alloys were studied by scanning electron microscopy. All the alloys studied show

DD FORM 1 JAN 73 1473 EDITION OF 1 NOV 65 IS OBSOLETE
S/N 0102-014-6601 |

SECURITY CLASSIFICATION OF THIS PAGE *(When Data Entered)*

similar galvanic current characteristics as a function of time, with an initially high current density which falls of to a stable value, primarily due to the accumulation of calcareous deposits on the cathodes. The corrosion patterns developed by each alloy are distinctly different, both on the macroscopic and microscopic scale. The commercial alloy Galvalum I macroscopically exhibits attack preferentially on specimen edges, while Reynode II tends to form vertically elongated dissolution cavities on the broad specimen surfaces, and KA-90 tends to profusely pit. These different behaviors can be rationalized in terms of the observed anodic polarization characteristics of the respective alloys. All the alloys show distinct crystallographic attack on the microscopic scale, but the details of dissolution morphology are quite different for each alloy.

INTRODUCTION

Currently, several producers are developing and marketing aluminum sacrificial anode alloys for application in marine cathodic protection systems. The research described in this report was initiated to develop a more detailed understanding of the corrosion behavior of some commercially available and developmental aluminum sacrificial anode alloys. In this study, a total of six different alloys were investigated, supplied by three different producers.

Several experimental approaches were applied in order to characterize the behavior of the subject materials. These experiments were designed to: (1) establish the time-dependence of galvanic current for different aluminum anode alloys when coupled to HY-80 hull steel and immersed in seawater; (2) characterize the polarization behavior; (3) utilize surface microanalytical techniques such as scanning electron microscopy and energy dispersive x-ray spectroscopy in order to study details of the corrosion processes of the different alloys; (4) discover if any of the alloys exhibit inhomogeneous attack or passivation effects that might hinder practical application as sacrificial anodes for marine cathodic protection.

Prior to discussing experimental procedures and results, a brief summary of previous research on aluminum anodes will be presented.

Previous Research on Aluminum Sacrificial Anode Alloys

The United States Navy has long been aware of the importance of effective cathodic protection for its ships hulls, and for some time has relied on military specification zinc anodes to afford this protection (1). Microscopic aspects of the anodic corrosion performance of these zinc anodes have received attention in previous research at the Naval Postgraduate School (2,3). In recent years (since 1973) zinc anode systems on some U. S. Navy surface ships have been replaced with impressed-current cathodic protection systems and there are indications that U. S. Navy plans are to eventually install impressed-current systems on a large proportion of surface ships (4). Aluminum sacrificial anodes apparently will see little if any application for hull protection; rather, it is expected that aluminum anodes will be used in accordance with General Specifications for Ships of the United States Navy,

Section 633, that is, to protect machinery, bilges, engineering space, structural supports and other internal areas of the ships (4).

It has long been realized that aluminum possesses the primary attributes needed by a sacrificial anode, namely: (1) potential sufficiently electronegative to provide adequate current flow, (2) high electrical output per pound of anode consumed, and (3) low cost. However, pure aluminum cannot be utilized as a sacrificial anode because of the protective oxide surface layer which forms on it and limits its current output (5,6). Some early alloy development work was partially successful in overcoming the detrimental effects of the oxide film (7), but the alloys were inconsistent in their electrochemical behavior and had a much lower efficiency than the theoretical 1352 ampere-hours per pound of pure aluminum (8).

To date, the major contributors in the field of research pertaining to aluminum sacrificial anode alloys have been the producers and users of the product. Since systematic research on this subject started in the 1960's, an assortment of basic and empirical work has been accomplished in the fields of electrochemistry and physical metallurgy. A major thrust to develop improved aluminum sacrificial anode alloys began when the economics of the metals market indicated possible advantages to a shift from conventional zinc- and magnesium-based alloys to aluminum-based materials (9). Also, with the proliferation of off-shore oil-drilling platforms in the 1970's, the aluminum industry had greater justification to conduct active research to improve and market economical and useful aluminum alloy sacrificial anodes. Such research has been conducted by producers in Europe (10-14), Japan (15), and the United States (5-9, 16-29), including basic alloy development work (5, 7, 8, 11, 15, 17, 20, 26, 28), and large scale testing of these alloys in laboratory and field conditions (6, 9, 10, 12-14, 16-19, 21-28). In the mid-1960's, the United States Navy began to evaluate the utility of aluminum sacrificial anode alloys for Naval vessels, this research being centered at the Naval Research Laboratory (8, 30-33). This work has recently led to a preliminary Military Specification for aluminum anodes (34).

On the standard EMF series, aluminum is between magnesium and zinc in electronegativity; but for a galvanic series in seawater it is less active than both magnesium and zinc because of passivation by a surface film (6). Since research had shown that magnesium and zinc could be made more active

by additions of mercury (11), some experimenters believed that mercury added to aluminum would make it more active and prevent passivation (8). However there was a major problem in producing an aluminum-mercury alloy, since a very minute amount of free mercury in contact with aluminum is a potent catalyst for the formation of aluminum oxide. Since it was of considerable interest to develope a mercury-bearing alloy in order to maintain an active surface on an aluminum sacrificial anode, Rachlot, in 1963, developed a method to alloy small amounts of mercury with aluminum without occurence of the catalytic reaction mentioned above, by use of a pre-alloy of magnesium-zinc-mercury (11). This pre-alloying scheme is now a proven method of introducing mercury to sacrificial aluminum alloy compositions.

As late as 1966 there was only limited information available on the effect of various alloy additions on the performance of aluminum as a sacrificial anode. Most of the experimentation involved large numbers of empirical observations (5-29). For example, Reding and Newport (Dow Chemical) reported that over 2500 alloys were processed and evaluated in order to be able to produce an anode with a high enough efficiency to be marketable (5). Reding and Newport made extensive studies of the effects of alloying elements added singly and in combination to aluminum, and determined that gallium, tin, indium, zinc, magnesium, barium, cadmium and mercury caused aluminum to exhibit a potential more active than unalloyed aluminum, and that the required concentrations of the alloying elements were quite small (5). Of course, the effect of each alloying constituent was somewhat different; for instance, mercury-bearing alloys had efficiencies on the order of 90-95%, while some tin-bearing alloys exhibited only 30% efficiencies. When the various favorable elements were combined in various proportions and added to aluminum, Reding and Newport (5) found that aluminum-mercury-tin and aluminum-mercury-zinc, consistent with Rachlot's conclusions, showed a high efficiency, approximately 95% (1290 ampere-hours per pound of aluminum alloy). At this point extensive macro-scale seawater testing was started on the aluminum-mercury-zinc alloy by Dow Chemical Company and the Navy (8,31).

Recently, a major concern to governments and commercial shippers has been the possibility of mercury contamination of the environment due to mercury-bearing alloys. Even though the mercury content is typically less

than one-half of one percent, this was and is a legitimate concern. Therefore, some research has been devoted to finding alternate aluminum alloy compositions with suitable efficiency. Sakano, Toda and Hanada (15) found that an anode with long continuing activity and high current efficiency could be prepared by the addition of indium and zinc to aluminum, and Reding and Newport (5) also noted that indium was a possibly favorable addition to aluminum. However, it was some years before Dow Chemical marketed an aluminum-indium-zinc anode (Galvalum^{R} III) (28,29). Sakano, Toda and Hanada (15) introduced the alloying elements to the melt in a "pre-alloy" form and galvanic efficiencies of about 92% were obtained. Smith, et al. (28) reported 88% efficiency for an aluminum-indium anode ten years after the Japanese work. These efficiencies compare favorably with the 95% efficiency figure reported by Reding and Newport (5) for aluminum-mercury anodes.

One difficulty with the aluminum-indium-zinc alloy was the development of irregular corrosion patterns over the test anode surfaces, both in field and laboratory studies (15). Various alloy additions were tested to try to increase the uniformity of corrosive attack, and eventually cadmium in small amounts (0.01-0.02%) was found to be useful for this purpose (15). The distribution of corrosive attack on the macroscale is important because, after all, an anode must be attached to the structure it is to protect; and if the area around the attachment is consumed at a higher rate than the remaining portion of the anode, there is a distinct possibility that the anode will fall from the structure long before it provides its full output. Also, it has been reported that mercury-bearing anode alloys, although most efficient, sometimes exhibit localized corrosive attack at unpredictable sites on the anodes and could conceivably result in (dramatically) decreased protection in the long term.

It has been pointed out that aluminum-mercury-zinc anodes typically show efficiencies greater than 90%, and that when compared to the military specification zinc anode, the aluminum anode is about 3.5 times as efficient (30). However, electrochemical efficiencies and corrosion patterns of some anode alloys, such as aluminum-zinc-tin, have been sometimes found to have such wide variation that their reliability for cathodic protection systems was considered questionable (33). In 1976, Jensen (Ship Research Institute of Norway) agreed with the concern,

expressed in NRL findings, that aluminum anodes could fall off protected structures. Jensen (10) reported that some anode users (ship and drilling-rig owners) were asking whether any aluminum anodes behaved "as advertised," a concern reported to be especially true in the case of aluminum-mercury-zinc anodes.

In view of these various statements regarding aluminum anode alloys, many of which have been incompletely supported by data, the present research was undertaken to characterize and compare the corrosion behavior of presently available alloy compositions. Especially it was intended to make both macroscopic and microscale observations of the corrosion phenomena, and to attempt to correlate the results, as much as possible, with the previous research reviewed above. It was of interest, for example, to ascertain whether some of the categorical "reputations" of certain alloy types were justified. It should be noted that the U. S. Navy has apparently already decided, on the basis of empirical studies (8,30-33), what type of aluminum anode alloy should be used aboard surface vessels, and a preliminary military specification has been drafted (34). However, in the conception of this study, it was verified (35,36) that information on the microscopic behavior of various anodes would certainly provide basic insight and might even be of practical use, such as contributing to the iterative process of alloy development.

At the outset of this research, the following questions were delineated as being of interest and importance to the understanding and performance of aluminum sacrificial anode alloys.

1. Do aluminum anode alloys that have similar alloy constituency (e.g., aluminum-mercury-zinc), but are produced by different manufacturers, experience the same form of corrosive attack (on the macroscale) and have similar dissolution patterns (on the macroscale)?

2. Do the microstructural characteristics of the alloys, such as affected by casting and/or heat treating processes, affect the corrosion mode and morphology?

3. Exactly what is the distribution and mode of corrosive attack on the various alloys?

4. What is the relation between microscale corrosion processes and galvanic current output?

5. Can the utilization of small specimens in a limited test program

provide information that can be correlated with large-scale field tests?

6. If information relating to basic differences between the corrosion behavior of the various alloys can be obtained, can this information be utilized to make viable decisions relative to the utility of the various alloys, and in what circumstances it is necessary to go to full-scale field tests?

7. What are the polarization characteristics of the various alloys, and what is their relationship to, and correlation with, the modes of corrosive attack and galvanic current output?

8. What are the corrosion products formed on sacrificial aluminum anode alloys in seawater?

EXPERIMENTAL METHODS

Representative samples of three basic types of commercially available aluminum anode alloys, i.e., aluminum-mercury-zinc, aluminum-tin-zinc, and aluminum-indium-zinc alloys were obtained with the assistance of Dow Chemical U.S.A., Reynolds Metal Company and Kaiser Magnesium Comapny. Six different alloys were obtained for study in this research. The trade names and nominal chemical compositions of these proprietary alloys are given in Table I. Samples for galvanic current measurements and polarization determinations were machined from this material. After some initial experiments involving all six alloys, three of the alloys were selected for more detailed study. Most of the results reported here relate to these three alloys, which were Galvalum I (here designated as alloy G-I), Reynode II (alloy R-II), and KA-90 (alloy K-90).

Galvanic current tests were conducted for each of the six alloys, coupled to HY-80 steel in quiescent synthetic seawater, and the aluminum members of these couples were subsequently studied microscopically. The six alloys were studied in (duplicate) galvanic couples for times up to fourteen days. The three alloys studied in more detail than the others, alloys G-I, R-II, and K-90, were subjected to a more rigorous matrix of time-interval immersions of from fifteen minutes to 96 hours.

Design of the cells for galvanic current measurements was quite simple. The apparatus used consisted of an array of 3000 ml beakers, each containing 2500 ml of artificial seawater, with oxygen saturation accomplished by

continuous aeration. The aluminum specimens were machined to 0.48 in. x 0.48 in. x 0.20 in. (1.22 cm x 1.22 cm x 0.51 cm) coupons, while the steel cathodes were 3.25 in. x 3.25 in. x 0.13 in. (8.25 cm x 8.25 cm x 0.32 cm), giving a surface area ratio between opposing faces of approximately 46:1 and a total area ratio of 27:1 (steel to aluminum). The anode and cathode were placed in 3000 ml beakers of synthetic seawater, 4 in. (10 cm) apart with faces parallel, connected by 14 in. (36 cm) of insulated #12 solid copper wire (total resistance 1.85×10^{-3} ohms). Galvanic current was monitored with a clip-on d.c. milliammeter (Hewlett-Packard Model 428A). The surface condition of the aluminum anodes was a cleaned and rinsed 600 grit finish. The steel cathodes were ultrasonically cleaned in acetone and boiled in a solution of 20% NaOH and 200 g/l zinc dust for ten minutes, then cleaned with steel wool, rinsed with distilled water and acetone, and dried with warm air.

Potentiodynamic polarization determinations were conducted to determine the single metal corrosion rates and polarization characteristics of the aluminum sacrificial anode alloys in synthetic seawater. The potentiostat used was a Princeton Applied Research Model-331 Deluxe Corrosion Measurement System. A continuous scan potentiodynamic technique was used in which potential was scanned at 1.0 mV/sec from an active potential through E_{corr} (corrosion potential) to a noble potential. Specimens for polarization tests were right circular cylinders 0.375 in. (0.953 cm) in height and diameter. The surfaces of the specimens were finished with 000 grit paper using a standard procedure while mounted in a lathe. Prior to immersion in the corrosion cell, specimens were ultrasonically cleaned in acetone for five minutes, rinsed with deionized water and ethanol, and dried. Synthetic seawater was prepared by standard methods (40) and fresh electrolyte was utilized for each polarization run. The corrosion cell was filled with electrolyte to a height of 3.5 in. (9.0 cm), and nitrogen gas was introduced into the electrolyte through a regulated sparger. The corrosion cell was then placed on a magnetic stirrer for a five minute deaeration period prior to commencement of a polarization run. After the electrolyte was deaerated stirring was stopped and the specimen inserted. A standard time of two minutes was established between specimen insertion in the electrolyte and commencement of a polarization run, and other standard procedures were followed.

After various intervals of galvanic current measurement, and after some polarization runs, aluminum samples were examined by scanning electron microscopy and other microscopic methods. In order to minimize electron charging of the surface due to nonconductive corrosion products, a 40-50 A layer of gold was usually evaporated over the specimen surfaces. This technique was successful for all specimens except those (e.g., alloy K-90) which had significant corrosion product present, in which case the gold coating did not significantly improve resolution at high magnifications. Some specimens were not gold coated, so that they could be studied by microbeam energy-dispersive x-ray spectroscopy, using a Princeton Gamma Tech PGT-1000 system. Some sample surfaces were also examined by SEM after removing corrosion products by standard methods.

RESULTS AND DISCUSSION

Galvanic Couple Behavior

Galvanic current was monitored for 334 hours (14 days) for each aluminum alloy and for MIL-SPEC zinc. These galvanic current vs. time curves were used as a basis of comparison with the predictions of potentiodynamic polarization curves. Also, visual and microscopic observations of the galvanically exposed samples were correlated with trends exhibited by they galvanic current vs. time curves. The galvanic current behavior (Figures 1-3) was very similar for the three alloys tested. However, distinctly different macroscopic corrosion patterns and microscopic dissolution morphologies were observed. Macrophotographs of the anodes and cathodes after these immersion tests are shown in Figures 4 and 5, respectively.

The galvanic current vs. time data demonstrate that the aluminum anodes have a relatively high initial galvanic current density compared to MIL-SPEC zinc (for the same area ratio with steel cathodes). MIL-SPEC zinc shows an initial current density of approximately 3mA/cm^2, while for alloy G-I the initial value is about 4.5 mA/cm^2, for alloy R-II about 7.4mA/cm^2, and for alloy K-90 about 8.4mA/cm^2. The particularly high initial current density for alloy K-90 is correlated with a high density of pits that form on the surface of the specimens within fifteen minutes of immersion. The aluminum sacrificial anode alloys all exhibit the same

general trend of galvanic current, with a high starting current density which rapidly decreases to a stable value. The decrease in galvanic current with time is not entirely attributable to a passivation phenomenon on the anode surface; it is also due to the buildup of calcareous deposits on the coupled cathodes (see Figure 5), which reduces the cathodic area which the anode has to protect, thereby lowering the required galvanic current output.

Although the galvanic current exhibits very similar trends for the various alloys there are distinctly different macroscopic corrosion patterns (Figure 4) and microscopic dissolution morphologies. MIL-SPEC zinc (Figure 4a) shows a more uniform pattern of corrosion than do any of the aluminum alloys, with no local dissolution cavities. The surface of the zinc anode becomes covered with a powdery white corrosion product, which has been determined to consist of an array of microscopic zinc oxide crystal platelets (2,3). The mercury-bearing alloys examined, except alloy G-II (Figure 4c) show attack that is free of corrosion product buildup, at least insofar as can be discerned on the macroscale. Alloys G-I, R-II, and K-95 (Figures 4b, 4e, and 4g respectively) develop similar patterns of attack, with a form which has been reported as typical of mercury-bearing anode alloys (8, 30-33), consisting of large areas of general dissolution, with other areas of the surface void of significant corrosion, or corrosion product. In contrast, alloy G-II becomes uniformly covered with a fragile white corrosion product (Figure 4c).

Alloys G-I and R-II, although similar in composition (both mercury-bearing), show distinctly different distributions of attack over the surface. Alloy G-I (Figure 4b) corrodes primarily along the edges of the specimen, while alloy R-II (Figure 4e) forms a set of parallel elongated dissolution cavities which grow by "worming" vertically down the broad faces. These two alloys have approximately the same alloy composition, but alloy R-II is reported to be "heat treated" after casting. Therefore, it may be inferred that the heat treatment of alloy R-II, as compared to the simple chill casting of alloy G-I, must account for the distinct differences in corrosion patterns observed for these two alloys. While the exact mechanisms accounting for the different behaviors cannot be described, it is likely that the heat treatment effect is realized in terms of the location of alloying elements in the respective microstructures. This

contrast in behavior between two compositionally similar commercial anode alloys serves to point out that factors other than alloy composition can be of great importance in aluminum sacrificial anode alloys, as demonstrated in this case when comparing the macroscopic corrosion patterns. The base metal microstructures of the G-I and R-II alloys are shown in Figure 6.

The macroscopic appearance of alloy K-90 (mercury-zinc-tin) after fourteen days exposure is illustrated in Figure 4f. The specimens are coated with a white, brittle corrosion product which when dried and scraped from the specimens reveals a uniformly corroded surface. The structure of the underlying corroded anode is brittle, and relatively large areas of it can be easily chipped off. The texture of the corroded anode is grainy and coarse, consistent with an attack mechanism involving severe intergranular corrosion. Subsequent high-magnification observations confirm this.

One might ask whether observations on these small-scale anode coupons can be related to the behavior of full-scale sacrificial anodes. In fact, the behavior is often remarkably similar, such as is seen when comparing the macroscopic appearance of specimens studied in this research (Figures 4a through 4g) with the macroscopic appearance of large scale field test specimens (Figure 4h) (41). In spite of the difference in scale, each commercial alloy is readily identifiable by its own unique pattern of corrosion.

The steel cathodes which are galvanically connected to the anodes became covered with calcareous deposits, and a large amount of flocculent precipitate forms and settles out in the seawater, collecting in the bottom of the cells. Figure 5 is a collection of macrophotographs of the various cathodes, with the calcareous deposits remaining on them after some of the loose-adhering deposits were removed for x-ray diffraction analysis. Cathodes galvanically coupled to alloys R-II and K-90 had more deposits on them than cathodes coupled to the other aluminum alloy anodes. It is well known that seawater, containing predominately sodium chloride, also contains significant amounts of bicarbonates and sulphates, and that these compounds are important in the corrosion process because they act as cathodic inhibitors, (42-44). Under quiescent conditions, as in the present galvanic couple tests, calcium carbonate and other compounds may be precipitated at the cathodic areas; and if the deposits adhere to the cathodic surfaces,

the cathodic process will be stifled. The calcareous deposits effectively reduce the area of the cathode and therefore reduce the anodic current output required for adequate cathodic protection. This factor contributes to the reduction in galvanic current output with time, observed for all the aluminum anode alloys tested. This may be particularly important in the case of the alloy anodes which do not become covered with corrosion product, i.e., alloys G-I, G-III, R-II, and K-90.

X-ray diffraction analyses were conducted on the deposits removed from the cathodes that had been galvanically coupled to the G-I, R-II, and K-90 anodes. These analyses were not totally conclusive, but there was good correlation with peaks of calcium carbonate and dihydrous calcium sulphate ($CaSO_4 \cdot 2H_2O$). According to LaQue (44), the typical composition of calcareous deposits found on steel cathodes immersed in seawater includes calcium carbonate and calcium sulphate, plus various other bicarbonates, sulphates and water. The variable proportion of water bound in the compounds causes difficulty in identification by x-ray diffraction. While complete identification of all compounds in these deposits was not possible, it was observed that the cathodic deposits for all the different anodes have qualitatively identical x-ray diffraction patterns, which indicates that the deposits are of the same identity, independent of the coupled anode alloy.

Formation of an opaque, flocculent precipitate in the seawater was observed in about the same proportion as the calcareous deposits on the cathodes; that is, couples involving alloys R-II and K-90 tend to form the most precipitate. The electrolyte from the various galvanic cell solutions sued were subsequently filtered to collect the precipitate, and x-ray diffraction patterns were run. However, the very fine powder material did not produce coherent x-ray diffraction patterns, indicating that it is either an amorphous substance, or (more likely) if crystalline, the particle size is so small that the x-ray peaks are smeared out.

When the initial (fourteen-day) galvanic current studies were completed three alloys were selected for more detailed study: alloys G-I, R-II, and K-90. Alloys G-I and R-II were selected because of their similar mercury content but different origin; also, both meet the alloy constituency percentages indicated in the preliminary military specification (34); alloy K-90 was selected because it displays a higher initial galvanic current, has a different alloy constituency, and has a distinctly different character in terms of distribution of attack and corrosion product formation.

Potentiodynamic Polarization Behavior

The potentiodynamic polarization behavior of alloys G-I, R-II, and K-90 is shown in Figures 7 a, b, and c. The behavior of alloy G-I is quite similar to that of alloy R-II (Figure 7b), while that of alloy K-90 (Figure 7c) is somewhat different. These potentiodynamic polarization curves, obtained from freely corroding single metal samples, can be used to predict the corrosion potential and current when the metal is galvanically coupled. Since in practical applications, aluminum anodes are galvanically coupled to more noble materials (in these experiments, to HY-80 steel), it was of interest to see if the independent potentiodynamic polarization curves of the coupled metals would predict the actual corrosion rates experienced by the aluminum anodes in the galvanic current tests. The polarization curve for HY-80 steel is shown in Figure 7d. Calculations were made for a cathode-to-anode surface area ratio of 27:1, the ratio of the total surface area of the steel plate cathode to the total surface area of the aluminum anode. The intersections of the cathodic branch of the HY-80 steel polarization curve with the anodic branch of the aluminum anode curves (for an area ratio of 27:1) are marked by an asterisk on Figures 7 a, b, and c. The polarization data for freely corroding aluminum sacrificial anode specimens is summarized in Table II, along with the predicted galvanic values and corrosion rates and the actual measured galvanic corrosion rates. Correlation between the actual weight loss measurements and calculations from galvanic current vs. time curves is extremely good for all three anode alloys. Correlation between the actual weight loss measurements and rates predicted from the potentiodynamic polarization data is within an order of magnitude. For instance, the predicted corrosion rate for alloy G-I predicted from polarization data is 165 mdd, while the rate measured from weight loss is 698 mdd.

The characteristics of the potentiodynamic polarization curves (Figures 7 a, b, and c) can be related to the macroscopic anodic behavior observed for the respective alloys. For example, because of the way the polarization curves interact with HY-80 steel (at area ratio 27:1), it would be predicted that anodes of alloys G-I and R-II would not experience significant pitting. On the other hand, because of the transpassive intersection of the polarization curves for alloy K-90, significant pitting of the anode would be predicted. The polarization curves for alloys G-I and R-II

(Figures 7 a and b) show that a relatively large potential must be applied in order to obtain the transpassive, or pitting, region of the anodic branch of the polarization curve. In contrast, the polarization behavior of alloy K-90 does not show an abrupt transition to a transpassive region during anodic polarization. The implication of this is that alloy K-90 will more readily obtain a profuse pitting condition when coupled to a given cathode. These predictions are validated by scanning electron microscope observations (Figures 8 a, b, and c) and macrophotographs (Figures 4 b, e, and f) of the aluminum anode specimens.

Microscopic Observations

A difficulty faced by those interested in improving cathodic protection systems is a lack of information concerning the actual corrosion mechanisms involved. While there is an abundance of data relating to the macroscopic findings of large scale corrosion testing, the corrosion process actually takes place on a microscopic level. In order to scrutinize the corrosion mechanisms of aluminum sacrificial anode alloys, scanning electron microscopy (SEM) was used extensively in the present research to study the surfaces of aluminum anode alloys after various anodic exposures. The high mangification direct observations afforded by SEM provide the researcher with unique information with which to develop ideas about corrosion mechanisms.

Low Magnification Observations: Initiation and Progress of Corrosive Attack

At relatively low magnifications (20X to 100X), Figures 8, 9, and 10 illustrate the distribution and progress of dissolution attack on the surfaces of alloys G-I, R-II, and K-90, respectively, after fifteen-minute exposures in (area ratio 27:1) couples with HY-80 steel. Figure 8 shows that alloy G-I exhibits initial dissolution localized along specimen edges, as noted earlier. On the other hand, the local dissolution of alloy R-II begins at an array of sites on the broad surface faces (Figure 9). Alloy K-90 (aluminum-tin-zinc) demonstrates much more profuse pit formation over the entire specimen surface, as illustrated by Figure 10 which shows numerous pits on the order of 30 μm in diameter.

Aluminum exposed to air forms an oxide film, generally considered to by γAl_2O_3. This film is regarded as a protective coating which also prevents aluminum and its alloys from corroding in seawater. One of the

questions addressed by the present research was: At the microscopic level, what mechanisms lead to breakdown of the passivating film and the start of pit formation on aluminum anodes when coupled to steel and immersed in artificial seawater? In fact, the attack modes observed on the various alloys in this work do not all constitute classical pitting, which we may define as rapid localized corrosive action with deep penetration and insignificant weight loss. Among the three aluminum alloys examined here, only alloy K-90 appears to be attacked by a "true" pitting mechanism, i.e., the attack of alloy K-90 resembles classical pitting whereas that of alloys G-I and R-II does not.

It has been pointed out that in terms of polarization behavior, an anode initially subjected to high current density, or an anode that requires only a small potential increase above its corrosion potential to obtain the transpassive (pitting) regime of its anodic polarization curve, tends to experience rapid pit formation, followed by lateral growth, or local dissolution around the pits (45). In this research alloy K-90 has the highest initial current density, and as evidenced in Figure 10, develops the largest number of pits per unit surface area. Therefore we see that the potentiodynamic polarization behavior of alloy K-90 directly correlates with the microscopically observed behavior, supporting the concept that ready attainment of transpassive behavior is associated with enhanced pit formation.

When comparing the surface attack in Figures 8, 9, and 10, it is seen that quite different anodic dissolution mechanisms are involved in the initial corrosive behavior of the three alloys, and an explanation for these diverse behaviors cannot be found in any unified theory for pitting. Alloys G-I and R-II have very similar alloy compositions, but alloy R-II is heat treated after a chill-casting to resolution zinc and mercury, then air cooled (46). It would thus be logical to assume that initial dissolution of alloy R-II, tending to locate on the broad surface faces rather than the edges of the specimens, is related to some effect of the heat treatment. The important alloy constituents, e.g., mercury, copper and iron, are nominally present in similar amounts in alloys G-I and R-II, but these elements are clearly not distributed the same in these two alloys. It is not obvious whether the effect is macroscale of microscale. That is, there may be differences in concentration on the macroscopic scale across the ingots from which the samples were machined, i.e., segregation from edge-to-center, or there may be differences in the distribution of alloying constituents in the microstructures of the respective alloys. It seems likely

that a different sensitivity to surface flaws and geometric discontinuities contributes to the different behavior of alloys G-I and R-II, i.e., the broad-surface dissolution attack on alloy R-II as opposed to the edge-localized attack on alloy G-I. This is suggested because the specimens of the two alloys were prepared in exactly the same way, so that the initial surface condition of all specimens was the same, yet alloy G-I exhibits dissolution indicating greater sensitivity to macroscopic geometric discontinuities and edge effects, while alloy R-II is insensitive to such features.

As previously noted, alloy K-90 anode specimens exhibit rapid and profuse pit formation of a more classical type over the entire surface (Figure 8c). The initial pits on alloy K-90, such as seen in Figure 10, are approximately 25-30 μm in diameter after fifteen minutes of galvanic action. As the immersion time increases, pitting action continues, and more pits are generated. This nucleation of more pits is in contrast to the tendency of the two other alloys studied, which are mercury-bearing. Research by Pryor, Keir, and co-workers (7,47) indicated that tin will reduce the corrosion resistance of an aluminum oxide (γ-Al_2O_3) film if the tin is evenly dispersed in the aluminum substrate, as it apparently is in the heat treated alloy K-90. It has been pointed out that only about 0.1% tin can be retained in a metastable solid solution but that homogenized aluminum-tin alloys containing greater than 0.1% tin will still corrode quite uniformly when coupled to steel and in a sodium chloride solution (7). Alloy K-90 nominally contains 0.12 - 0.20% tin, and does corrode "evenly", i.e., shows pitting attack that is uniformly distributed over its surface.

It appears that a variety of mechanisms initiate the corrosion process on different aluminum sacrificial anode alloys. In the case of the alloys studied in this work, it is somewhat arbitrary, when observing the various modes of attack, as to what should be considered classical pitting and what should be considered as simply local dissolution. It was decided that the dissolution sites formed on alloys G-I and R-II do not propagate by a classical pitting mechanism; instead they enlarge as "local dissolution cavities." However in the case of alloy K-90, the high initial current density, together with the particular polarization behavior, alloy homogenization, and environmental factors, contribute to localized breakdown of the aluminum oxide film, and a true "pitting" mechanism operates.

In these materials, we are also interested in the manner in which the various alloys corrode after initial pit formation. It is seen from the current vs. time curves (Figures 1, 2, 3) that the electrochemical properties of the galvanic couples change with time. Galvanic current, which starts at a relatively high value for all the anode types, rapidly decreases and then maintain itself at an apparently stable value. In term of the associated surface dissolution processes, we observe that initial pits grow into larger "local dissolution cavities" or propagate as "true pits," and distinct surface morphologies become evident on the dissolution surfaces when viewed at high magnification (discussed in next section). Within the first twenty-four hours of immersion, a number of similar macroscopic aspects of corrosion are exhibited by the three aluminum sacrificial anode alloys, including the following:

(1) the corrosion process decreases the total mass of each anode but increases the surface area;

(2) calcareous deposits form on the cathodes;

(3) corrosion products form, to various extents, on the anodes;

(4) large amounts of white flocculent matter precipitate in the seawater.

All these physical phenomena influence the net corrosion behavior of the aluminum anodes. Some of these factors initially tend to stifle the anodic reaction, but the galvanic current supplied by the anodes eventually obtains a stable level rate. It is of interest to determine how the galvanic current is able to be supplied under the apparently changing conditions related to the corrosion process. In order to pursue this question it is necessary to move to a consideration of more microscopic aspects of dissolution and corrosion product formation.

High Magnification Observations: Microscopic Dissolution Behavior

Figures 11, 12, and 13 illustrate the typical microscopic surface structure of the respective alloys after various immersion times. These views, at magnifications from about 100X to more than 1000X, show that typically anodic attack is localized, and is realized on the microscopic scale by processes of crystalline dissolution. This is the case for all three alloys, although the details of the dissolution morphology differ for each.

Galvalum I (Alloy G-I): Microscopic characteristics of the corrosive attack mode of alloy G-I are illustrated in Figure 11. Alloy G-I shows initial dissolution from the edges of the specimens inward. Dissolution is more rapid along the edge of the specimen, somewhat slower inward from the edge. The process undercuts the general surface film to a slight extent as it progresses. At high magnification (Figure 11b, 11e) it is noticed that there is a distinct crystallographic nature to the dissolution surface morphology, which is virtually free of coverage by any corrosion product. We have applied the term "herringbone" to the unique crystallographic dissolution pattern which develops on alloy G-I; the surface morphology consists of a set of hillocks of base metal extending outward from a central ridge, appearing much like ribs extending outward from the spine of a fish skeleton. Figure 11b particularly illustrates this herringbone pattern as seen at high magnification. The white "puffs" at the peaks of the "backbone" are corrosion product, while the hillocks, or rib-bones, extending from the central spine are base metal. In between the individual herringbone patterns are flattish valleys of more uniform metal dissolution. The rib-bones in such patterns are typically 2-3 μm in width and are separated by troughs that are 1-2 μm in width; these dimensions do not vary much with immersion time. This particular dissolution surface morphology was apparent on all specimens of alloy G-I studied, with the only variable being the amount of corrosion product, which increased with time. The morphological and dimensional consistency of these herringbone patterns reflects the particular dissolution mechanism of this aluminum sacrificial anode alloy.

To interpret the dissolution morphology in more detail, the crystallography of the face-centered-cubic (FCC) aluminum matrix must be considered. The atomic arrangement at a planar surface of a poly-crystalline solid varies with grain orientation relative to the section plane. In many metallic crystals, certain planes tend to be preferentially etched, leaving other planes geometrically evident (48). Since the close-packed planes of a crystal have the greatest number of atomic bonds distributed in them, these tend to be the type of faces revealed by etching; also if the bonding energy is plotted as a function of orientation in the plane (Wulff Plot), there is maximum energy in the direction of close-packing (49). For FCC crystals the close-packed planes are (111) and the close-packed directions are <110>.

Therefore, if aluminum is placed in an environment that will preferentially etch to reveal close-packed planes, the etching response of a given crystal (grain) depends on the plane of section through it. Vermilyea (50) reports that if the initial section plane is the (111) plane of an FCC crystal, this plane maintains a constant potential during an etch, but if the initial section plane is other than (111), the potentials of these other (non-close-packed) planes drift and approach that of the (111). This is accomplished by the other planes being rapidly etched until they approach the configuration of a (111) plane, and then the etching mechanism slows. From this process, distinct faceted morphologies are created, and microscopically, nearly the entire surface of the crystal becomes bounded by close-packed planes (50).

The grain boundary configuration seen at the upper right in Figure 11c clearly illustrates the "step structure" created on grain surfaces by preferential etching. The herringbone patterns also represent a step structure, with the spines and ribs formed by bounding close-packed (111) planes of the aluminum, and the preferentially etched areas between the rib-bones are planes of less dense atomic packing. The details of the dissolution model are discussed in a separate paper (51). The scale of the dissolution surface pattern does not change significantly with time. Figures 11d, 11e, and 11h illustrate the constant dimensionality of the herringbone pattern.

Base metal grain boundaries in alloy G-I are only very slightly undercut, i.e., they experience only a small increase in the degree of dissolution (Figures 11d and 11e). As time of immersion increases, slight penetration appears along certain boundaries, and outer grain surfaces become revealed due to differences in dissolution rates for different grain aspects. Therefore, we conclude that in this alloy, there is no tendency for grain boundaries to be corrosively attacked by a classical "intergranular corrosion" mechanism; the attack here is much more subtle in nature, similar to normal metallographic etching. Figure 11e shows the junction of three grains (seen in the center of Figure 11d) that display differing dissolution rates.

Figure 11f illustrates the typical appearance of the "uncorroded" areas of the surface of specimens after several hours' exposure. There is evidence of a continuous (but cracked) film (it is likely that the film cracked during drying) and small outcroppings of corrosion product. The continuous film is the aluminum oxide which initially covered the surface of the specimens.

The small corrosion product outcroppings are fairly tenacious, in that they do not readily rinse off the surfaces in distilled water.

As the immersion time for alloy G-I specimens increases, the amount of corrosion product that deposits on the dissolution surface increases to some extent (Figures 11g, 11h, 11i, and 11j). The corrosion product localizes on the spines of the herringbones (i.e., on the pointed edges of the step structure) in clusters and appears to be very fine crystallites. (Recall that no x-ray diffraction peaks were produced by the precipitate matter in the seawater.) The surface structure for alloy G-I immersed ninety-six hours is illustrated by Figures 11i and 11j, and shows continued prevalence of the herringbone pattern. The ribs (steps) remain 2-4 μm in width, with larger amounts of corrosion product on the central spines (major steps). The corrosion process continues to undercut unattacked surface areas of the specimen (Figure 11j); this points out that once the general film is broken and a dissolution region established, the film is no longer a significant factor. It is also noticeable in Figure 11j that a new film is beginning to form over the dissolution area; a "mud-cracked" pattern can be seen in it after drying.

After fourteen days coupled to steel, the surface of alloy G-I anodes was corrosively attacked over only about one-third of the area, in spite of the high edge-to-surface ratio of our test coupons. This emphasizes that the general corrosion behavior of alloy G-I involves localization of attack in slowly expanding dissolution cavities. Since the active surface area of the anode is actually increasing, and since little corrosion product accumulates on the attacked surface areas, the anode is corroding in a manner that allows it to continue to perform its current-providing function.

The base metal microstructure of alloy G-I is shown in Figure 6a. On the dissolution surfaces there is very little evidence of localized attack that might be associated with this microstructure. The microstructure reveals no second phases or compositional segregation. Figure 6a shows the large grain structure found in the center of the chill-cast "pencil" ingots which were machined to make the test specimens; the outer regions of the mechanical coupons did have somewhat smaller grains; this is evident in some SEM photographs (e.g., Figures 11a and 11d). The center grains of the chill-cast pencils are larger than 1.2 mm, while some grains on the edges of the immersion specimens are on the order of 0.2 mm in diameter.

It is possible, but not obvious, that the observed herringbone dissolution patterns are related to a base metal microstructural feature, perhaps a fine-scale dendritic pattern. Since the herringbone features are not observed on the dissolution surface of other alloys of similar nominal composition, a base metal microstructural origin is a possibility. But the effect may be less direct, such as through the effect of composition on the surface energies of crystallographic planes.

Reynode II (Alloy R-II): The typical microscopic corrosion features observed for alloy R-II are illustrated in Figure 12. This alloy exhibits its own characteristic dissolution patterns and fea ures, quite different from those exhibited by alloy G-I, although these alloys are similar in constituency. Alloy R-II samples typically exhibit rapid formation of local dissolution sites, (e.g., Figure 12a, 12d, 12e, etc.) followed by elongation (downward on vertical faces) into local dissolution cavities (termed "worm-pitting" as seen in Figure 9). Within the dissolution cavities, on a fine-scale, variable dissolution rates are seen for neighboring grains in a given region (Figure 12a),and a unique "peaked" structure is a prevalent microscale feature on the dissolution surfaces (Figures 12c and 12l).

As for alloy G-I, the dissolution areas on alloy R-II spread laterally, slightly undercutting the unattacked surface of the anode, as can be seen in Figures 12a, 12d, 12e, and 12m. The physical impression is that alloy R-II obtains the transpassive condition during polarization more easily than alloy G-I (see polarization curves, Figure 7), thereby forming an array of initial pits on its surface. Enlargement of these initial sites into elonggated dissolution cavities is facilitated by undercutting the passivating film on the surface of the specimens.

The series of photomicrographs in Figure 12 serves to illustrate the chronology of dissolution cavity growth for alloy R-II. The dissolution cavities grow and worm along the surface of the specimens, a macroscopic growth characteristic evident in Figure 9. The wormpits grow vertically down the anode surface during exposure, with much slower widening of the cavity. Apparently a gravity effect causes corrosion by-product to flow out of the local dissolution site, down the vertical face of the specimen, aiding in the progression of corrosive attack vertically downward.

At higher magnifications, the surfaces of the dissolution cavities show unique dissolution morphologies (e.g., Figures 12d and 12i) in which

the base metal grains and grain boundaries are clearly distinguished. Some grains show distinct sets of parallel facets, while others are without any particular characteristic. The most characteristic microscopic feature of the dissolution surfaces of Reynode II are dense clusters of cone-like peaks. The specific shape of these peaks depends on the grain aspect, and it is not clear whether they are a perfect octahedral form. Figure 12b is a magnified view of Figure 12a and shows a white crested structure (that runs diagonally across Figure 12b) corresponding to a base metal grain boundary. The projection of this grain boundary ridge above dissolved inner grains is typical and is the opposite of the tendency of alloy G-I, which exhibited a slight degree of grain boundary penetration. Note the array of peaks to the left of the boundary in Figure 12b. These peaks, also illustrated by Figure 12c are 2-4 μm in height and width and appear in a regular, uniformly-spaced array. Figure 12l also illustrates the distinct peak (octahedral) formation, for a twenty-four-hour exposure. Sometimes these peak features have a less distinct appearance, as seen in Figures 12k and 12j, where they appear rounded and worn.

As discussed earlier, most crystals develop faces of simple orientation when electrolytically etched, and the final face is independent of the orientation of the face initially exposed to the solution. The remaining faces are clearly the most slowly dissolved and very often are the close packed planes of the particular crystal structure. It is evident from Figure 12c that preferential etching attacks the base metal in this manner and works to develop the peaks, while at the same time leaving intervening plane surfaces, as in the center of the figure. Although both alloy G-I and alloy R-II form distinct crystallographic dissolution surface structures, there is a significant difference between the dissolution morphologies. The question is why, since these two alloys have similar composition, specimens from both alloys were made in the same manner, and all testing was accomplished with a standard procedure. The only known difference between alloy G-I and alloy R-II is that the latter is heat-treated after casting. This solution heat treatment apparently allows a redistribution of alloying elements that effects the dissolution morphology when the metal is corroded in a saline environment. The exact mechanism which leads to the observed differences in etched surface morphology is not known at this time. The base metal

microstructure of alloy R-II is shown in Figure 6b. A large average grain size (over 1.2 mm) is seen,comparable to alloy G-I (Figure 6a), but alloy R-II also shows a dendritic segregation structure within the grains.

Figures 12e and 12k give striking evidence of the grain orientation-dependence of dissolution in alloy R-II. The topological relief seen in Figure 12e reflects the fact that each of the grains in the field had a different corrosion rate. There is very little corrosion product present on any of the dissolved surface, a feature in common with alloy G-I and undoubtedly related to the mercury content of these alloys (11).

Another common dissolution morphology seen for alloy R-II is illustrated by Figures 12g and 12m, where the surface dissolution topology appears striated, meaning grooved or channeled. The striations do not cross grain boundaries, and are approximately parallel to each other within a given grain. This type of pattern is obviously an alternative dissolution morphology developed when certain grain aspects are presented to the electrolyte.

In summary, the predominant features of the dissolution surface of alloy R-II reflect preferred crystallographic etching, with dissolution morphologies resulting from the various dissolution rates of close-packed and non-close-packed crystal planes. The commonality between alloys G-I and R-II is that both materials develop initial local dissolution sites which expand laterally. However, the attack on alloy G-I concentrates initially at the edges of the specimens, while alloy R-II attacked primarily on the broad face surfaces. Also, both alloys expand their dissolution sites by undermining the general oxide layer on the surface.

KA-90(Alloy K-90): Microscopic characteristics of the anodic attack of alloy K-90 are shown in Figure 13. The predominant feature is a rapid, true pitting phenomenon, with a fine distribution of pits over the surface (many pits per unit area),as seen in Figure 10; these pits form profusely in the early stages of attack, and gradually grow and coalesce as time goes on. Once again, there is evidence of crystallographic dissolution. Faceting is seen within the various grains (e.g., Figure 13e, 13g, 13h) with the orientation of the facets different in each grain, reflective of the different aspects that the grains present at the planar surface. As dissolution proceeds, a tendency to intergranular corrosion (IGC) is noticed microscopically in alloy K-90 (Figure 13f) and is also evidenced when physically inspecting

specimens after immersion tests, at which time the specimen surfaces are observed to be loosely granular and tend to crumble. Figures 13e, 13f, 13g, and 13h illustrate the microscopic aspects of the intergranular corrosion of alloy K-90. In the center of Figure 13g, a large opening is seen at a base metal grain triple point. These dissolved openings sometimes progress completely between and around grains, and sometimes grains become covered by smooth, egg-shell-like capsules, as in Figure 13h.

The dissolution surface of alloy K-90 has a much heavier deposit of corrosion product, especially for short times, than alloys G-I or R-II (e.g., Figures 13a, 13b, 13c). In fact, the dissolution surface morphology is often obscured by these deposits. However, the deposits are not compact, and do not afford protection against attack of the anode. Figures 13c and 13d illustrate dissolution undermining of the unattacked surface of the anode. Figure 13d is particularly descriptive of this behavior, where the undermined surfaces of the anode can be seen hanging over the edges of a large pit. This mode of dissolution obviously avoids any problem of passivation created by a general surface oxide film, but does not impair the anode's ability to supply current and cathodically protect. In addition to becoming covered with a heavier corrosion product accumulation than do anodes of alloys G-I and R-II, alloy K-90 anodes develop heavier-than-average calcareous deposits on the associated cathodes. These calcareous deposits reduce the exposed cathode area requiring protection. In order to investigate further this behavior, it would be useful to study the behavior of these alloys as a function of cathode-to-anode area ratio.

As mentioned earlier, the pitting features seen in Figure 10 may be correlated with the alloy's high initial galvanic current; the high starting current breaks down the oxide film and allows pitting to begin The attainment of transpassive polarization behavior by alloy K-90 after relatively low polarization (see polarization curves, Figure 7) creates a situation that allows the cathodic branch of the HY-80 polarization curve to intersect the transpassive region of the alloy K-90 anodic polarization curve at relatively high current density. Thus, when alloy K-90 is coupled to HY-80 steel and immersed in artificial seawater, it pits profusely.

It is of interest to consider on a microscopic scale why alloy K-90 pits at a given location. Keir, et. al. (7) suggested that pitting may occur where there is a concentration of tin which breaks down the resistance of

the aluminum oxide film. By the same reasoning, if there is a concentration gradient near base metal grain boundaries, dissolution may proceed at these locations as an intergranular corrosion phenomenon. The microstructure of alloy K-90 is shown in Figure 6c. There is a subtle precipitate-free zone adjacent to the grain boundaries and precipitate particles distributed throughout the grains, with larger particles along the grain boundaries and at "triple" points. This is essentially the same microstructure as presented by Keir et. al. for an Al- 0.08% tin alloy (7); alloy K-90 has a 0.10% tin content. It is reasoned that local concentrations of tin, in conjunction with the high starting current and polarization behavior, create the necessary conditions for the macroscopic pitting behavior and microscopic dissolution attack mode of the alloy.

SUMMARY AND DISCUSSION

The three commercial aluminum sacrificial anode alloys studied in this work, show similar galvanic current characteristics as a function of time. Each alloy initially exhibits a relatively high current density (4.5 mA per cm^2 for alloy G-I, 7.4 mA per cm^2 for alloy R-II, and 8.4 mA per cm^2 for alloy K-90) which falls off to a stable level (approximately 0.8 mA per cm^2 for each alloy, in couples with steel at area ratio 27:1). Current density diminishes and stabilizes in this way primarily due to formation of calcareous deposits on cathode surfaces, which effectively reduce the surface area of the cathodes and so reduce the anodic current output required for adequate cathodic protection. Cathodes protected by alloy K-90 develop the heaviest calcareous deposits, and alloy K-90 anodes themselves become covered with more corrosion product (than alloys G-I or R-II). The corrosion product on the alloy K-90 anodes does not constitute passivation, i.e., does not impair the anode's ability to supply galvanic current. It is obvious that each anode material adequately protected the HY-80 steel to which it was coupled for the duration of the tests in this research, as evidenced by the continuing provision of galvanic current and by the calcareous deposits formed on the cathodes.

Macroscopic corrosion patterns exhibited by each alloy studied are different, related to compositional and thermal history variables of the alloys. For alloy G-I, which was chill-cast and not heat-treated, the distribution of dissolution sites over the samples shows greater attack at the

edges of the specimens; this indicates that this alloy is more sensitive to geometric effects (potential distribution). Alloy R-II, which is cast, heat-treated, and slow-cooled, shows formation of local dissolution sites on the broad surfaces of the anode. Although alloy R-II forms more local dissolution sites than alloy G-I, the heat treatment of alloy R-II apparently does not completely homogenize the alloy; the dissolution sites are not as numerous as those on alloy K-90, and cover only a fraction of the surface area of the anode; also, the microstructure of as-received alloy R-II indicates that the alloy is still dendritically segregated. Alloy K-90 is heat-treated at approximately 900^{o}F in order to re-solution tin and zinc, and then is water quenched; it typically shows rapid, widespread, fine-scale pitting. The initial pits expand and coalesce to eventually cover the entire specimen surface. In this case it is likely that the alloy composition is related to the pitting behavior through the influence of a fine-scale distribution of tin-rich precipitates in the base metal of this alloy, creating favorable sites for the start of the pits.

The small specimen coupons used in this study seem to fairly represent large anode samples, based on the fact that the same general corrosion patterns are seen over the surface of the small coupons as are seen on full-size anodes (41). This supports the validity of small-scale, inexpensive, laboratory tests for comparing aluminum anode alloys.

The dissolution patterns of mercury-bearing anodes could probably be improved by establishing alloying and heat-treating procedures to encourage more uniform corrosive attack. It is logical to assume (and it is apparent from the behavior of alloy K-90) that solution heat-treating increases the uniformity of macroscopic corrosion patterns. However, it still cannot be stated exactly what factors lead to localized corrosion attack of mercury-bearing alloys.

The experimental techniques used in this research (galvanic current, polarization, microscopy) have provided correlative results which establish an anode alloy's corrosion behavior. For instance, alloy K-90's high initial galvanic current density and polarization behavior provide evidence that the alloy will exhibit pitting attack. Observations by scanning electron microscopy and macrophotography have verified this behavior by providing physical evidence of pitting on alloy K-90 anodes. Also polarization and galvanic current data obtained from alloy R-II suggests that

this alloy will exhibit more pitting than alloy G-I and less than alloy K-90. Again, microphotography shows this to be the case.

Scanning electron microscope examinations of the corroded surfaces of aluminum sacrificial anode specimens show that a combination of corrosion mechanisms is responsible for the dissolution morphology. Each type of alloy investigated evidences its own particular microscopic dissolution pattern, with certain distinct morphological features. The dissolution morphologies exhibited are all quite obviously crystallographic, but the specific morphologies are different. Alloy G-I exhibits a unique "herring-bone" step pattern, with relatively small amounts of corrosion product on the dissolution surface, indicative that the alloy is not likely to passivate. Alloy R-II shows a completely different dissolution morphology from alloy G-I,which might not be anticipated since these two alloys are almost identical in nominal composition. There are two general features of the dissolution patterns of alloy R-II: (1) a dissolution morphology of "peaks" formed by preferential crystallographic etching (dissolution), and (2) variable dissolution rates for different grains within a single dissolution region. As for alloy G-I, alloy R-II samples show only small amounts of corrosion product (macroscopically and microscopically) so that a passivation problem would not be anticipated for this alloy. Alloy K-90 specimens do not show microscopic dissolution patterns which are as distinct as the "herringbones" and "peaks" associated with the other two alloys; but there is evidence of intergranular corrosion on the microscopic scale, consistent with the physical attributes of the specimens (crumbling of the surface).

In this work, the corrosion rates calculated from galvanic current data show quite good correlation with weight loss measurements. Also, the galvanic current data and potentiodynamic polarization data for those alloys are reproducible and can be used to predict the relative corrosion rates of aluminum anode alloys when galvanically coupled to other metals. In the course of this research, it has been shown that effective reproducible potentiodynamic polarization curves can be obtained routinely for these aluminum sacrificial anode alloys.

X-ray diffraction analyses carried out to try to identify corrosion products were inconclusive. X-ray powder patterns were obtained in an attempt to identify (in-place) the relatively heavy corrosion product on the

alloy K-90 anodes, calcareous deposits on the cathodes of galvanic couples, and a white flocculent precipitate which accumulated in the synthetic seawater electrolyte. X-ray diffraction patterns of the alloy K-90 corrosion product and the precipitate in the electrolyte were inconclusive, probably because these products were amorphous or (more likely) of very fine particle size. X-ray diffraction patterns of the calcareous deposits on the cathodes produced peaks corresponding to calcium carbonate and dihydrous calcium sulphate ($CaSO_4 \cdot 2H_2O$). The diffraction patterns produced from deposits on all cathodes were identical, irrespective of anode alloy.

Alloys G-I and R-II have similar alloy constituency but very different microscopic corrosion dissolution patterns. The reasons for this difference were not established during this research. It can only be conjectured that the heat treatment of alloy R-II and its additional quantity of zinc are the factors creating the different microscopic dissolution characteristics. This contrast in behavior between two compositionally similar commercial anode alloys serves to point out that factors other than alloy composition can be of great importance in aluminum sacrificial anode alloys.

REFERENCES

1. Military Specification MIL-A-18001H, Anodes, Corrosion Prevention, Zinc; Slab, Disc and Rod Shaped, 28 June 1968.

2. J. Perkins, W. H. Luebke, K. J. Graham, and J. M. Todd, "Anodic Corrosion of Zinc Alloys in Sea Water," J.Electrochem. Soc. 124 (1977) 819-826.

3. J. Perkins, and R. A. Bornholdt, "The Corrosion Product Morphology Found on Sacrificial Zinc Anodes," Corros. Sci. 17 (1977) 377-384.

4. Private communication with W. Strasburg, Naval Ship Engineering Center, November 1977.

5. J. T. Reding, and J. J. Newport, "The influence of Alloying Elements on Aluminum Anodes in Sea Water," Materials Protection, 15-18, December 1966.

6. C. F. Schrieber, and J. T. Reding, "Field Testing a New Aluminum Anode," Materials Protection, 33-36, May 1967.

7. D. S. Keir, M. J. Pryor, and P. R. Sperry, "Galvanic Corrosion Characteristics of Aluminum Alloyed with Group IV Metals," J. Electrochem. Soc. 114 (1967) 777-782.

8. T. J. Lennox, Jr., M. H. Peterson, and R. E. Groover, "A Study of Electrochemical Efficiencies of Aluminum Galvanic Anodes in Sea Water," Materials Protection, 23-37, February 1968.

9. L. S. Birnbaum, B. M. Taylor, and W. M. Strasburg, Jr., "Cathodic Protection," Nav Eng.J., 13-24, April 1971.

10. F. O. Jensen, "Corrosion and Protection of Offshore Steel Structure," Paper #182, presented at the National Association of Corrosion Engineers Convention, Houston, Texas, March 22-26, 1976.

11. B. Rachlot, "Sacrificial Anode Alloys -- Their Specifications and Uses," Proceedings of the Second International Congress on Metallic Corrosion, NACE, 285-289, 1966.

12. W. B. Mackay, "Deep Water Testing of Sacrificial Anodes," Materials Performance , 36-40, August 1974.

13. W. B. Mackay, "Deep Water Testing of Sacrificial Anodes (Part 2)," Materials Performance, 39-43, December 1975.

14. G. I. Russell and J. Banach, "Selection of Anode Systems for Cathodic Protection in Natural Waters," Materials Performance, 18-23, August 1971.

15. T. Sakano, K. Toda, and M. Hanada, "Tests on the Effects of Indium for High Performance Aluminum Anodes," Materials Protection, 45-50 December 1966.

16. G. W. Kurr, "Sacrificial Anode Applications in Ships," Materials Protection, 3-7, November 1969.

17. E. G. Haney and G. W. Kurr, "Sea Water Efficiency Tests on Aluminum Alloy Anodes Containing Zinc, Indium and Cadmium," Materials Performance, 27-30, May 1976.

18. C. M. Grandstaff, J. N. Schertzer, H. L. Graig, Jr., and K. G. Compton, Performance Evaluation of Quality Aluminum Anodes in Sea Water," Paper #110, presented at the National Association of Corrosion Engineers Convention, Chicago, Illinois, March 4-8, 1974.

19. K. G. Compton, "Cathodic Protection of Structures in Sea Water," Paper#13, presented at the National Association of Corrosion Engineers Convention, Toronto, Ontario, Canada, April 14-18, 1975.

20. G.L. Doremus, and J. G. Davis, "Marine Anodes: The Old and New, Cathodic Protection for Offshore Structures," Materials Protection, 30-34, January 1967.

21. G. L. Doremus, and J. G. Davis, "Modern Approach to Cathodic Protection of Offshore Pipelines," Pipeline Engineer, 36-45, October 1969.

22. E. P. Doremus, and R. B. Pass, "Cathodic Protection of 516 Offshore Structures - Engineering Design and Anode Performance," Materials Protection and Performance, 23-27, May 1971.

23. J. G. Davis, E. P. Doremus, and R. B. Pass, "New Aspects of the Application of Cathodic Protection to Offshore Facilities," Materials Performance, 9-15, September 1975.

24. F. E. Rizzo, and E. Bauer, "Cathodic Protection Current Distribution on Offshore Platforms," Paper #31, presented at the National Association of Corrosion Engineers Convention, San Francisco, California, March 14-18, 1977.

25. D. L. Johnson, "Diver Installed Anode Replacement Systems for Offshore Structures," Paper #32, presented at the National Association of Corrosion Engineers Convention, San Francisco, California, March 14-18, 1977.

26. J. T. Reding, "Sacrificial Anodes for Ocean Bottom Applications," Materials Protection and Performance, 17-19, October 1971.

27. J. T. Reding, and T. D. Boyce, T. D., "Cathodic Protection Performance of Offshore Anodes at a Simulated Depth of 600 Feet," Paper #111, presented at the National Association of Corrosion Engineers Convention, Chicago, Illinois, March 4-8, 1974.

28. S. N. Smith, J. T. Reding, and R. L. Riley, Jr., "Development of a Broad Application Saline Water Aluminum Anode - 'Galvalum'III," Paper#180, presented at the National Association of Corrosion Engineers Convention, Houston, Texas, March 22-26, 1976.

29. S. N. Smith, C. F. Schrieber, and R. L. Riley, Jr., "Supplementary Studies of the Galvalum III Anode - Exposure Time and Low Temperature," Paper #35, presented at the National Association of Corrosion Engineers Convention, San Francisco, California, March 14-18, 1977.

30. T. J. Lennox, "Electrochemical Properties of Magnesium, Zinc and Aluminum Galvanic Anodes in Sea Water," Proceedings, Third International Congress on Marine Corrosion and Fouling, 176-190, October 1972.

31. Naval Research Laboratory Memorandum Report 2300, The Electrochemical Characteristics of Aluminum Galvanic-Anode Alloys in Sea Water, by T. J. Lennox, Jr., R. E. Groover and H. H. Peterson, June 1971.

32. Naval Research Laboratory Report 7648, The Effect of Mercury and Tin from Aluminum Galvanic Anodes on the Corrosion Characteristics of 5086-H34 and 6061-T6 Aluminum Alloys in Sea Water, by T. J. Lennox, Jr., R. E. Groover and M. H. Peterson, November 16, 1973.

33. M. H. Peterson, T. J. Lennox, Jr., and R. E. Groover,"The Effect of Initial Low Anode Current Densities on the Subsequent Performance of Galvanic Anodes," paper presented at the National Association of Corrosion Engineers Convention, Toronto, Ontario, Canada, April 14-18,1975.

34. Military Specification (Preliminary), Anodes, Corrosion Preventive, Aluminum, draft of 1 November 1974, prepared under project No. 5340-N060.

35. Private communication with Mr. Ray Lindberg of Reynolds Metal Company, March 1977.

36. Private communication with Mr. Jack Schrear of Kaiser Magnesium Company, April 1977.

37. R. L. Leroy, "Evaluation of Corrosion Rates from Polarization Measurement," Corrosion 31 (1975) 173-177.

38. P. E. Morris, and R. C. Scarberry, "Predicting Corrosion Rates with the Potentiostat," Corrosion 28 (1972), 444-452.

39. "The Reproducibility of Potentiostatic and Potentiodynamic Anodic Polarization Measurements," an ASTM G-1/X1 Interlaboratory Testing Program, prepared by ASTM Committee G-1, Subcommittee X1, Task Group 2, Materials Research and Standards, 25-26, September 1969.

40. D. R. Kester, I. W. Duedall, D. N. Conners, and R. M. Pytokowicz, "Preparation of Artificial Seawater," Limnology and Oceanography, 12 (1967) 176-178.

41. KA-90 and KA-95, Aluminum Anodes for Cathodic Protection in Marine Environments, Kaiser Aluminum and Chemical Corporation, 1977.

42. H. H. Uhlig, Corrosion and Corrosion Control, John Wiley & Sons, 1971, 334-350.

43. H. T. Rogers, Marine Corrosion, George Newnes Limited, 1968, 272-283.

44. F. L. LaQue, Marine Corrosion, Causes and Prevention, John Wiley & Sons, 1975, 104-106.

45. J. A. Richardson, and G. C. Wood, "The Study of the Pitting Corrosion of Al by Scanning Electron Microscopy," Corros. Sci. 10 (1970) 313-323.

46. Private communication with Coleman Grandstaff of Reynolds Metal Company, Richmond, Virginia, on November 3, 1977.

47. M. J. Pryor, "Contribution to a Discussion on 'A Study of the Pitting Corrosion of Al by Scanning Electron Microscopy' by J. A. Richardson and G. C. Wood," Corros. Sci. 11 (1971) 463-464.

48. C. Edeleanu, and J. G. Gibson, "Influence of Crystal Structure on Corrosion," First International Congress on Metallic Corrosion, Butterworths, 1962, 72-77.

49. P. Bennema, "Generalized Herring Treatment of the Equilibrium Form," Crystal Growth; An Introduction, P. Hartman, ed., North-Holland Publishing Company, 1973, 342-347.

50. D. A. Vermilyea, "What I'd Like to Know about Corrosion," First International Congress on Metallic Corrosion, Butterworths, 1962, 62-71.

51. J. Perkins and J. R. Cummings, to be published.

Table I:

Galvalum® I*:	0.047%Hg
(Alloy G-I)	0.45%Zn
	0.019%Cu
	0.034%Fe
Galvalum® II*	0.048%Hg
(Alloy G-II)	0.0018%Cu
	3.0%Zn
	Fe - not determined
Galvalum® III*:	0.0156%In
(Alloy G-III)	2.9%Zn
	0.13%Si
Reynode® II**:	1.25-2.0%Zn
(Alloy R-II)	0.03-0.06%Hg
	0.003%(max)Cu
	0.07%(max)Fe
KA-90®***:	6.0-7.4%Zn
(Alloy K-90)	0.12-0.20%Sn
	<0.1%Fe
	<0.1%Si
	<0.005%Cu
KA-95®***:	1.2%Zn
(Alloy K-95)	0.5%Hg
	<0.1%Fe
	<0.1%Cu

Obtained from: *Dow Chemical U. S. A.

**Reynolds Metal Company

***Kaiser Magnesium Company

TABLE II

Potentiodynamic Polarization Data and Corrosion Rate Predictions for Single Metal Aluminum Alloys and Couples with Steel

Single Metal Data						Measured and Calculated Corrosion Rates for Aluminum:Steel Couples (Area Ratio 1:27)					
Material	i_{corr} ($\mu A/cm^2$)	E_{corr} (V_{SCE})	R_{mpy}	R_{mmpy}	R_{mdd}	Couple	i_{couple} ($\mu A/cm^2$)	E_{couple} (V_{SCE})	R_{mpy}	R_{mmpy}	R_{mdd}
Alloy G-I	8.4	-1.37	3.6	0.090	6.7	Alloy G-I/ HY-80 (P)	202	-0.90	88	2.2	165
						(W)			349	8.7	655
						(G)	858		372	9.2	698
Alloy R-II	4.1	-1.16	1.7	0.043	3.3	Alloy R-II/ HY-80 (P)	172	-0.91	73	1.9	140
						(W)			409	10.6	781
						(G)	916		391	10.1	746
Alloy K-90	3.7	-1.19	1.5	0.038	2.9	Alloy K-90/ HY-80 (P)	3530	-0.97	1720	43.7	3390
						(W)			760	19.3	1500
						(G)	1220		595	15.1	1170

NOTE: Data marked (P) are predicted from the potentiodynamic curves. Data marked (W) are from immersion test weight loss data. Data marked (G) are derived from the galvanic current curves for actual couples.

LIST OF FIGURES

Figure 10: Low-magnification scanning electron micrographs of KA-90 anode coupons after various times coupled to HY-80 steel (area ratio 1:27) in synthetic seawater. (a) 0.5 hrs., 60X, distribution of initial dissolution sites on broad face of specimen, (b) 1.0 hr., 20X, (c) 12 hrs., 20X, (d) 24 hrs., 20X, (e) 48 hrs., 60X, note accumulation of corrosion product near dissolution sites.

Figure 11: Scanning electron micrographs of dissolution morphology of Galvalum I anodes (a) 1 hour, 120X, regular pattern evident in each base metal grain, (b) 1 hour, 1200X, magnified view of region, showing characteristic "Herringbone" step pattern of dissolution morphology, (c) 1 hour, 600X, note steps on grain at upper right, (d) 2 hrs., 250X, note directionality of dissolution surface pattern in each grain, (e) 2 hrs., 650X, grain boundary evident on dissolution surface, (f) 4 hrs., 2300X, cracked compact film on uncorroded region of anode surface, (g) 24 hrs., 220X, "herringbone" step structure in dissolution region, with an increase in the amount of corrosion product (white clusters): note slight undercutting of general surface film, (h) 24 hrs., 2000X, magnified view of corrosion product clustering on steps of dissolution surface, (i) 96 hrs., 230X, (j) 96 hrs., 600X.

Figure 12: Scanning electron micrographs of dissolution morphology of Reynode II anodes (a) 0.5 hr., 200X, ridges evident along grain boundaries within dissolution region, (b) 0.5 hr., 1000X, magnified view of grain boundary ridge near center, (c) 0.5 hr., 1000X, magnified view of grain surface, showing characteristic "peak" morphology, (d) 1 hr., 250X (e) 1 hr., 500X, note distinct definition of grain surface facets (f) 1 hr., 1000X, "peak" morphology evident at high magnification, (g) 2 hrs., 500X, striated morphology evident on some grain surfaces (h) 2 hrs., 1000X, "peak" morphology (i) 4 hrs., 100X, (j) 4 hrs., 1000X, (k) 8 hrs., 1000X, (l) 24 hrs., 1000X, (m) 72 hrs., 600X, note striated dissolution morphology in some grains, peak morphology in others.

Figure 13: Scanning electron micrographs of dissolution morphology of KA-90 anodes. (a) 0.5 hr., 1200X, dissolution cavity undercutting surface and corrosion product buildup, (b), 1 hr., 600X, surface of dissolution cavity, (c) 2 hr., 1200X, dissolution cavity, (d) 12 hrs., 240X, dissolution cavities; note surface undercutting, (e) 24 hrs., 1200X, note striated step structure on dissolution surface; this structure is only evident when corrosion product falls away from the surface, (f) 24 hrs., 600X, note grain triple point accented by concentrated attack along grain boundaries, (g) 24 hrs., 2400X, close-up of grain triple point, showing grain line penetration, (h) 24 hrs., 1200X, encapsulation of grains by smooth corrosion product shells.

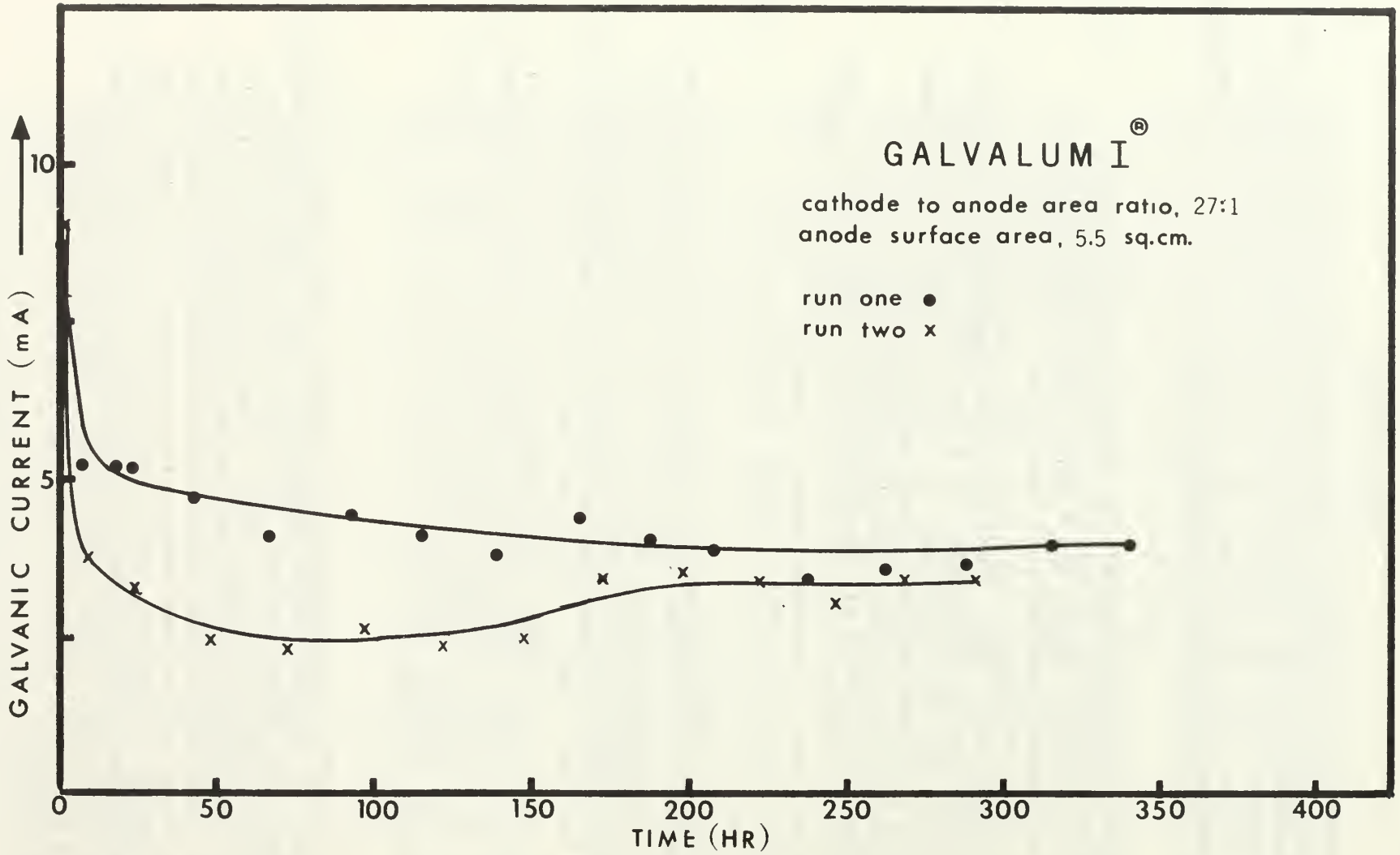

Figure 1 (a): Galvanic current vs. time behavior of Galvalum I/HY-80 steel couples (area ratio 1:27) in synthetic seawater over initial fourteen-day period.

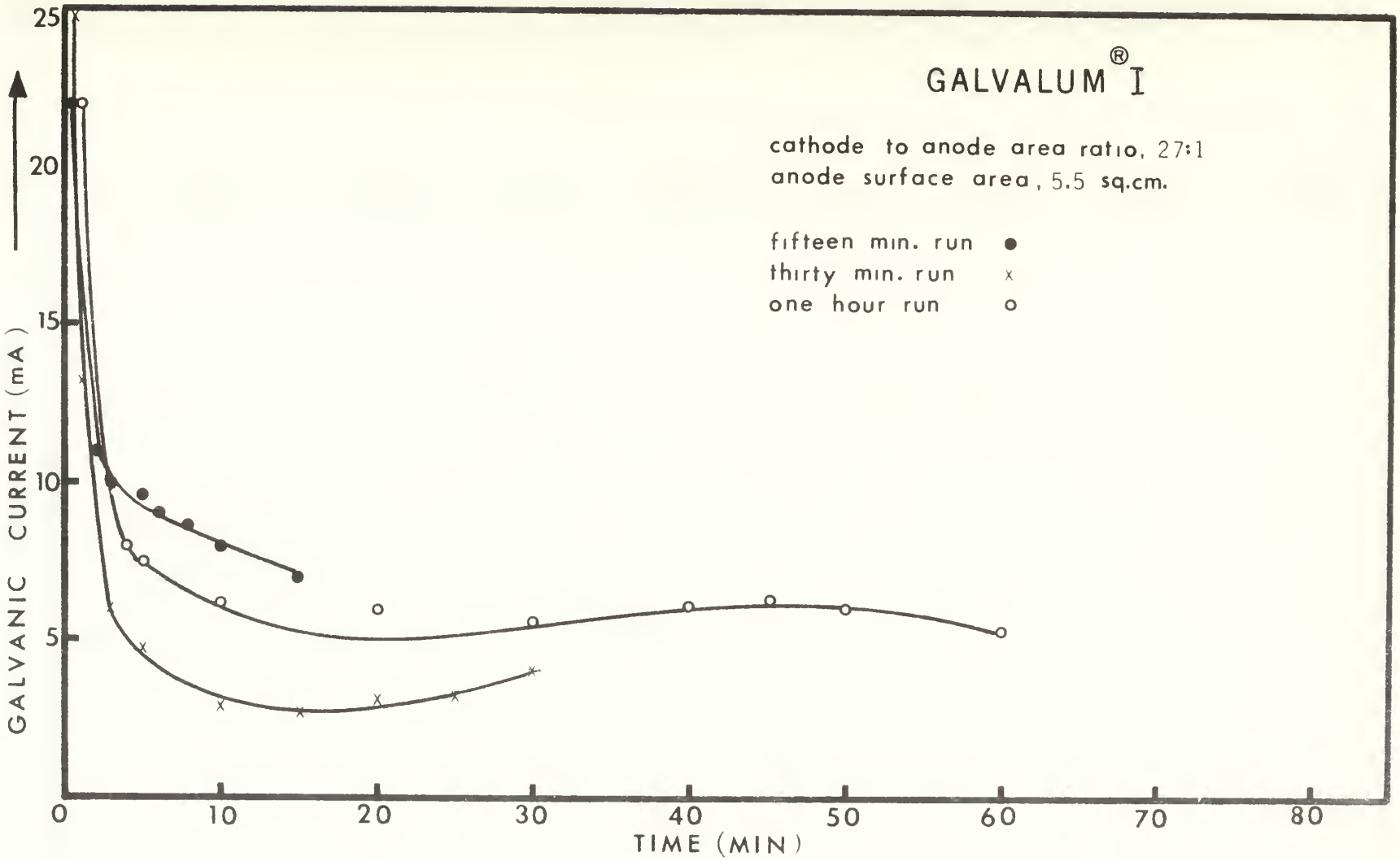

Figure 1 (b): Galvanic current vs. time behavior of Galvalum I/HY-80 steel couples (area ratio 1:27) in snythetic seawater at very short times.

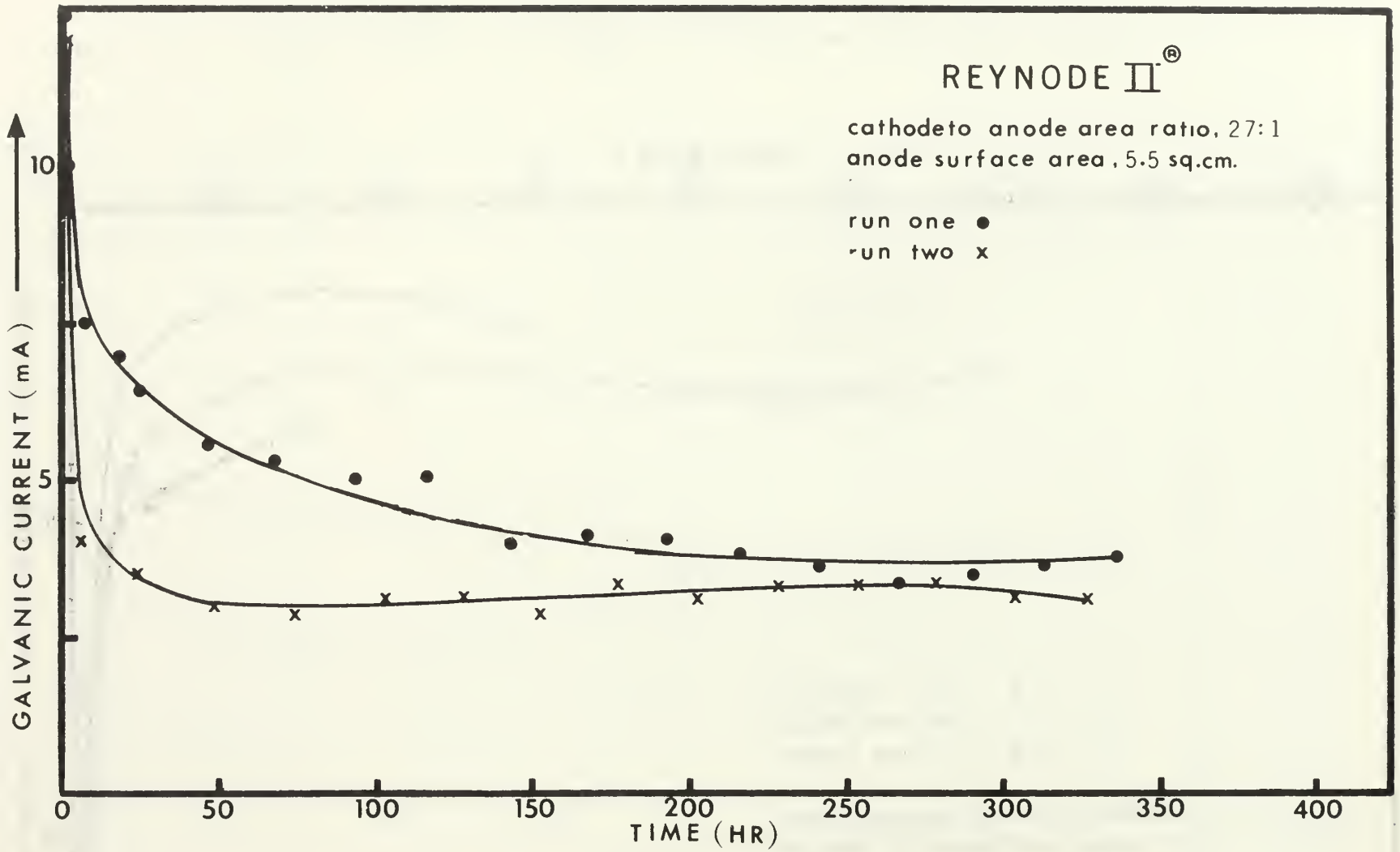

Figure 2 (a): Galvanic current vs. time behavior of Reynode II/HY-80 steel couples (area ratio 1:27) in synthetic seawater over initial fourteen-day period.

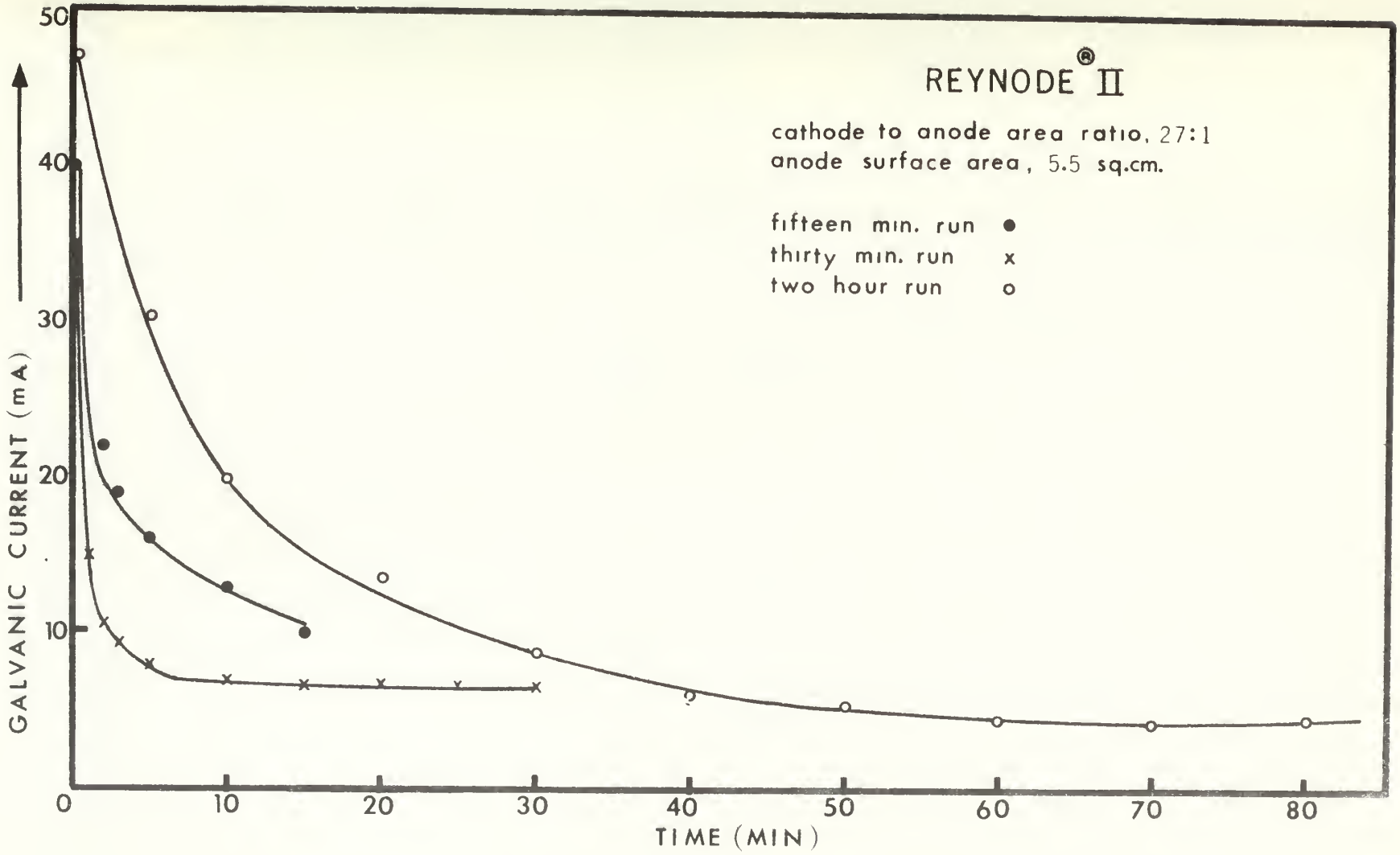

Figure 2 (b): Galvanic current vs. time behavior of Reynode II/HY-80 steel couples (area ratio 1:27) in synthetic seawater at very short times.

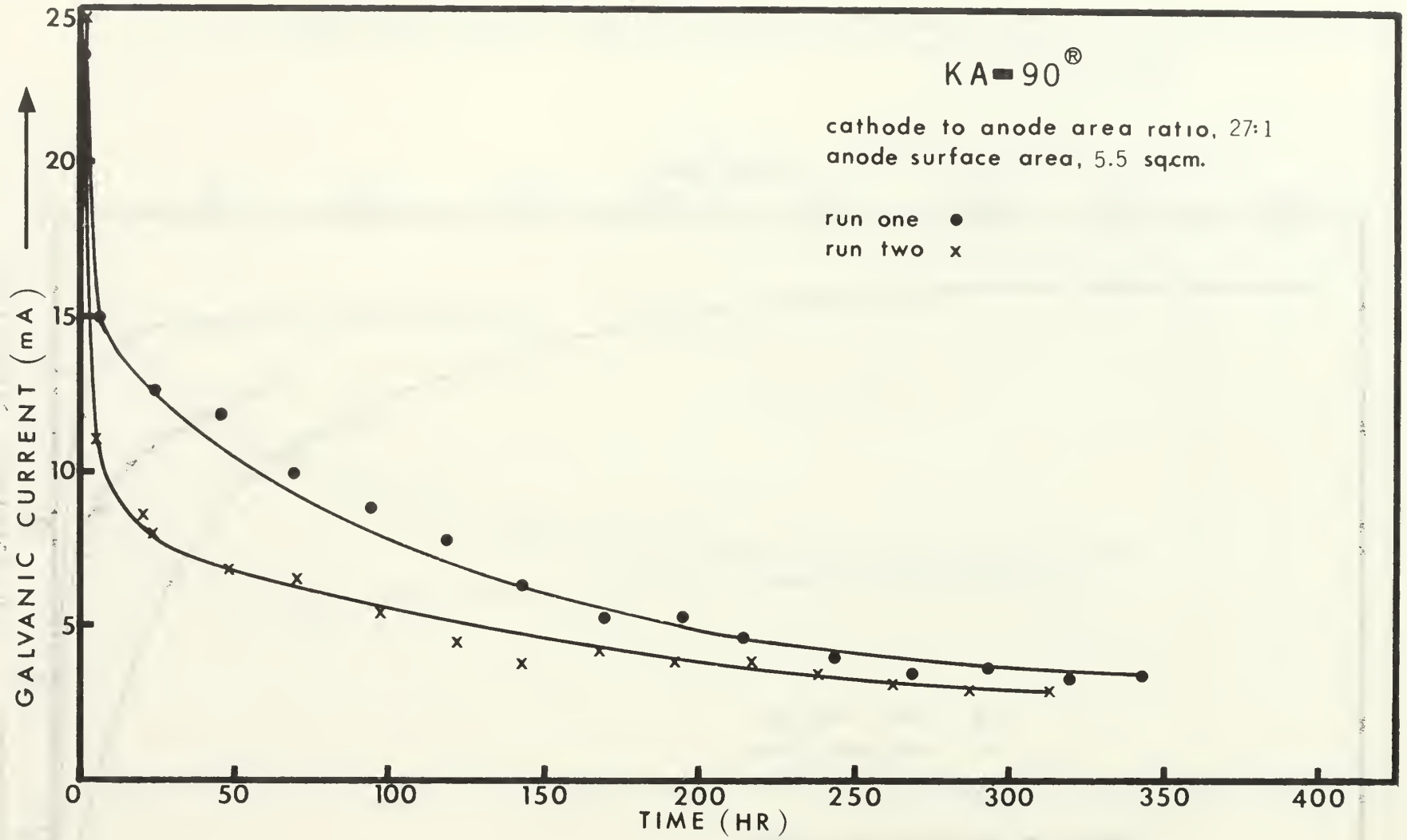

Figure 3 (a): Galvalum current vs. time behavior of KA-90/HY-80 steel couples (area ratio 1:27) in synthetic seawater over initial fourteen-day period.

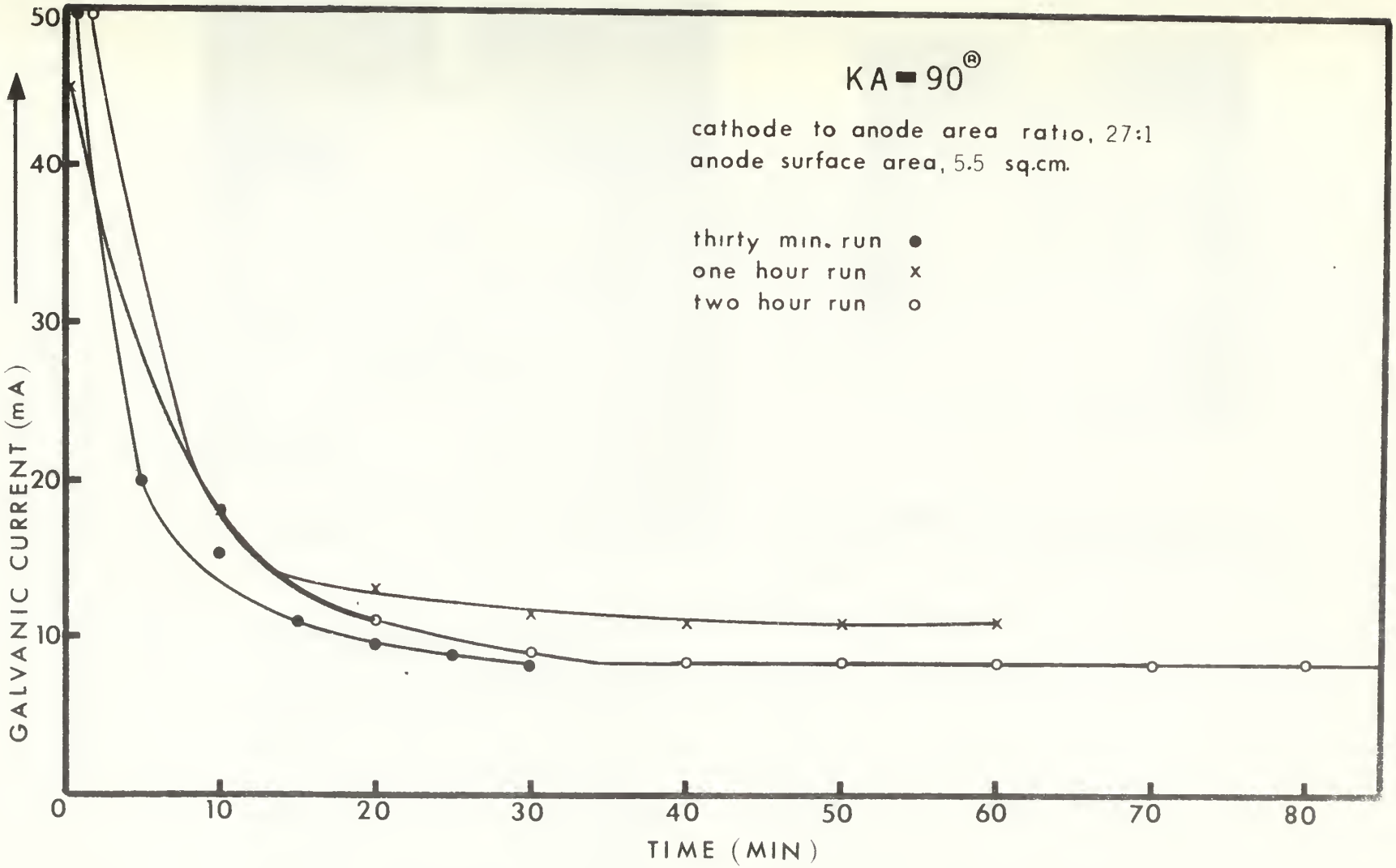

Figure 3 (b): Galvanic current vs. time behavior of KA-90/HY-80 steel couples (area ratio 1:27) in synthetic seawater at very short times.

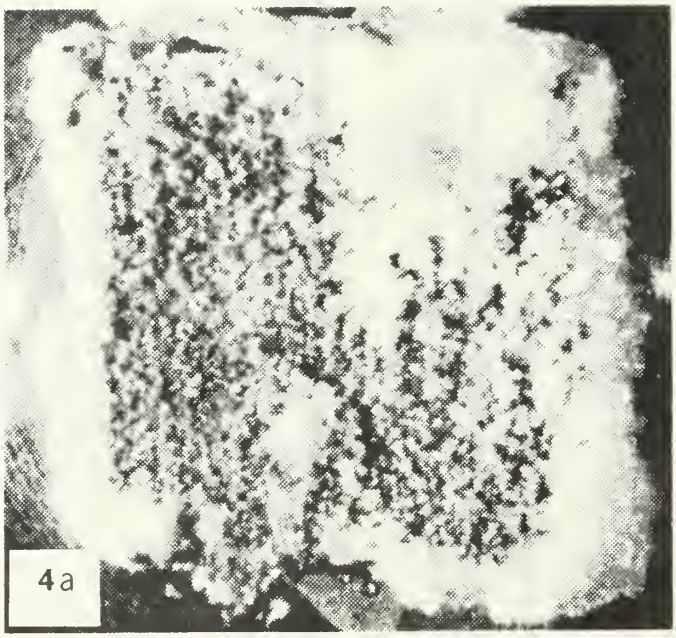

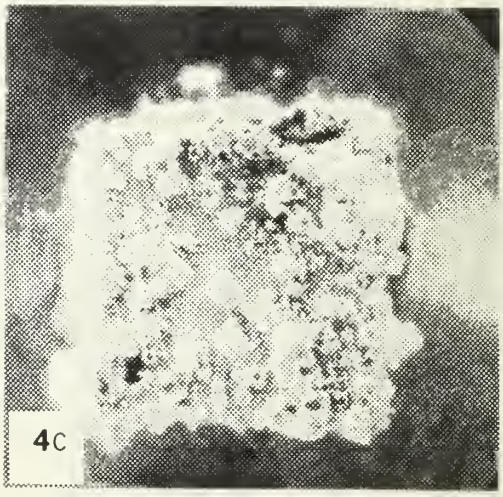

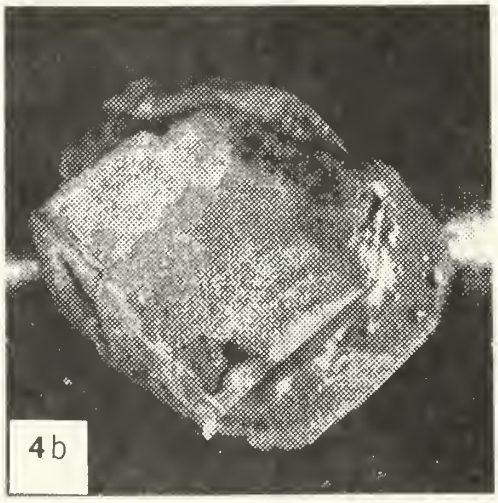

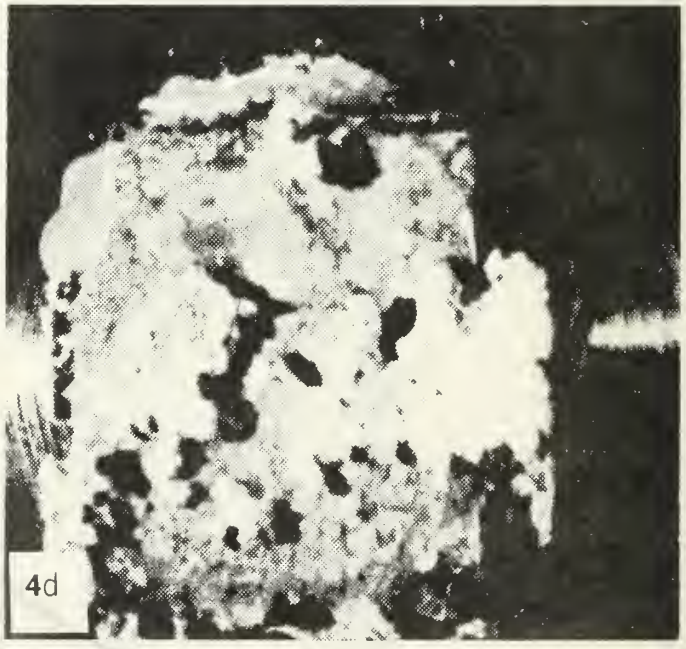

Figure 4: (a-g) Photographs of coupon anodes (1.22 cm x 1.22 cm x 0.51 cm) after 14-days coupling to steel (area ratio 1:27) in synthetic seawater. (a) MIL-SPEC Zinc (b) Galvalum I (c) Galvalum II Galvalum III (e) Reynode II (f) KA-90 (g) KA-95.

4e

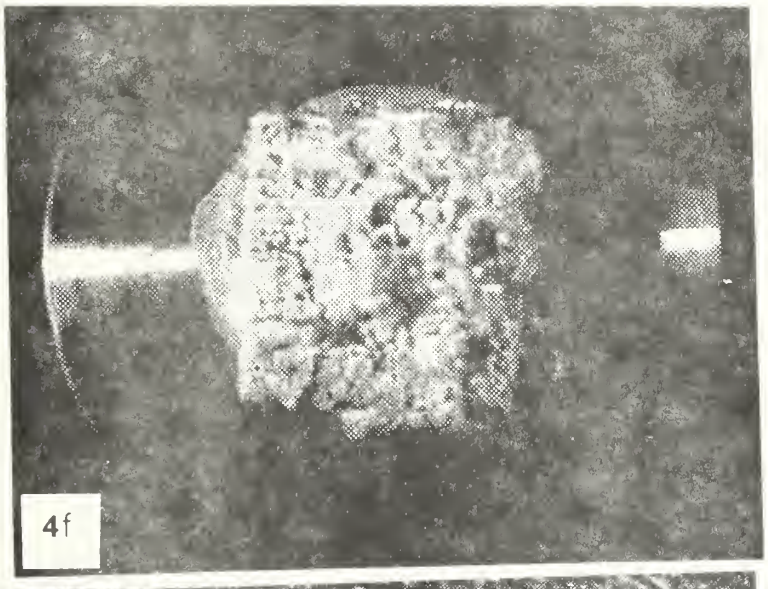

4f

4g

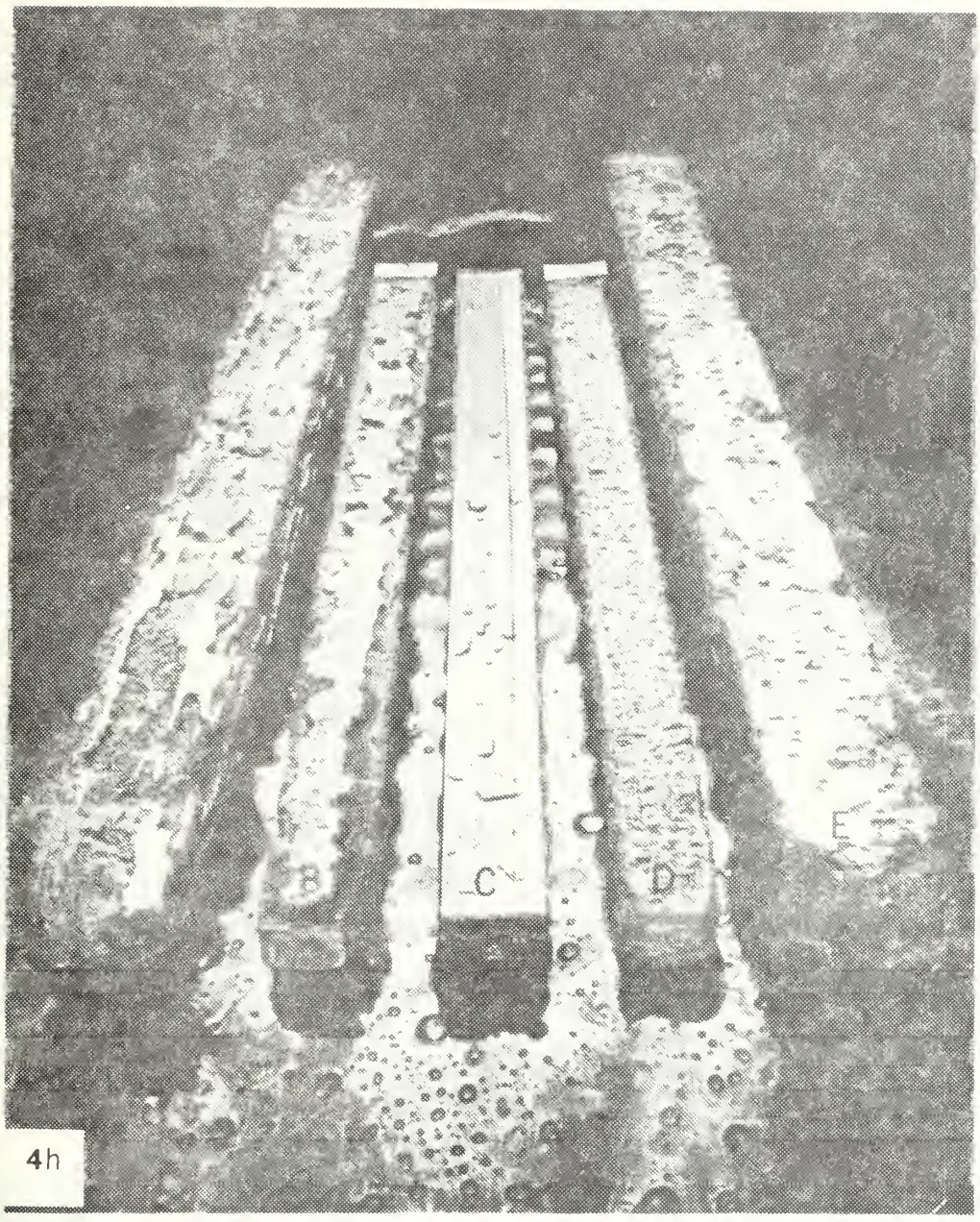

Figure 4 (h): Photograph of full-size sacrificial aluminum anodes (3.8 cm x 3.8 cm x 38 cm): the alloys shown, left-to-right, are A: Reynode II, B: KA-95, C: unexposed anode, D: KA-90, E: Galvalum I. Photograph courtesy of Kaiser Aluminum.

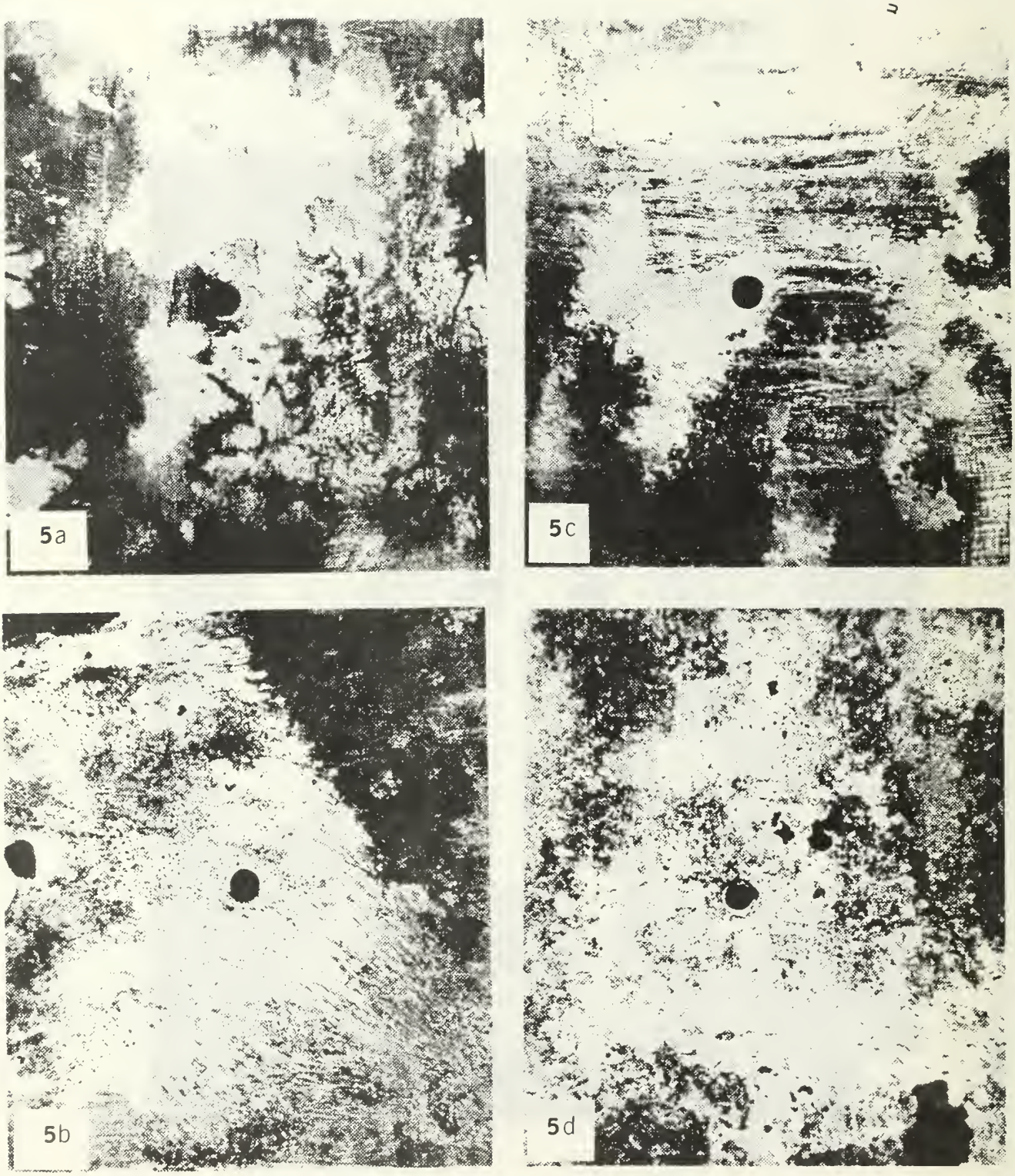

Figure 5: Photographs of HY-80 steel cathodes (8.25 cm x 8.25 cm x 0.32 cm) after 14-days coupling to anodes (area ratio 27:1) in synthetic seawater; the associated anodes were: (a) MIL-SPEC Zinc (b) Galvalum I, (c) Galvalum II, (d) Galvalum III, (e) Reynode II, (f) KA-90, (g) KA-95.

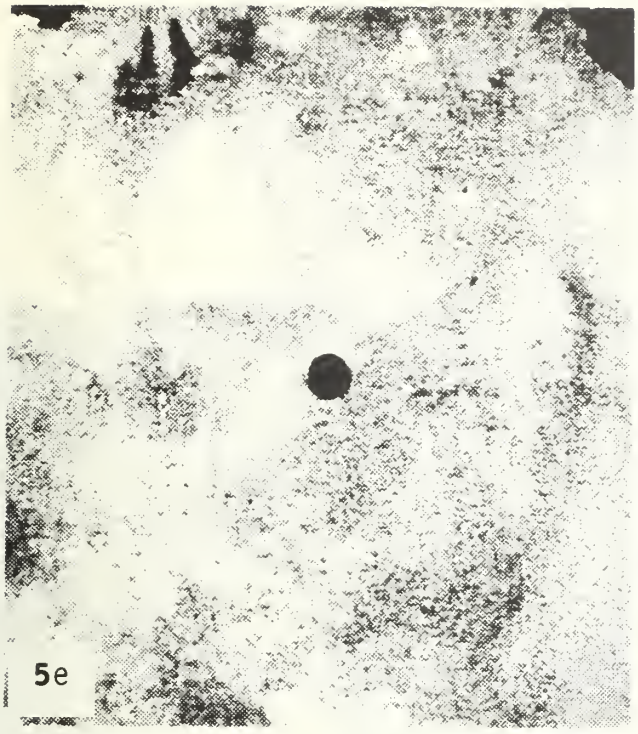

5e

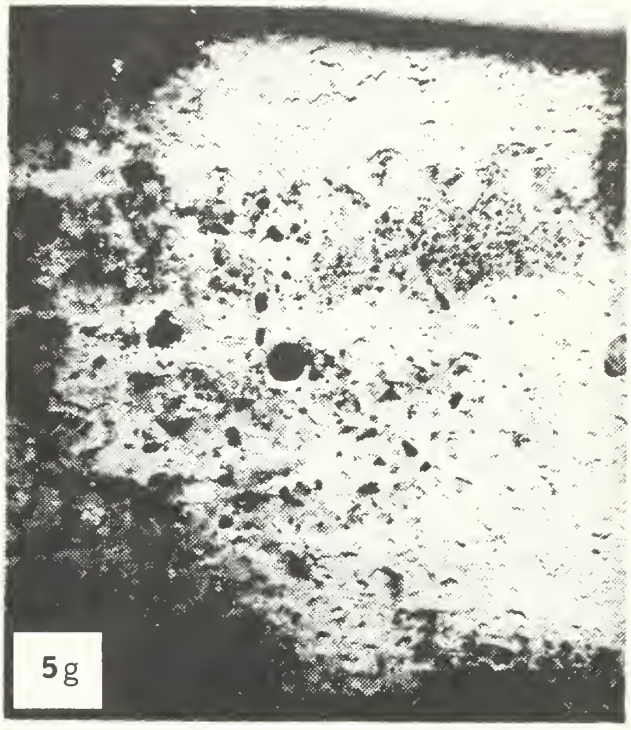

5g

5f

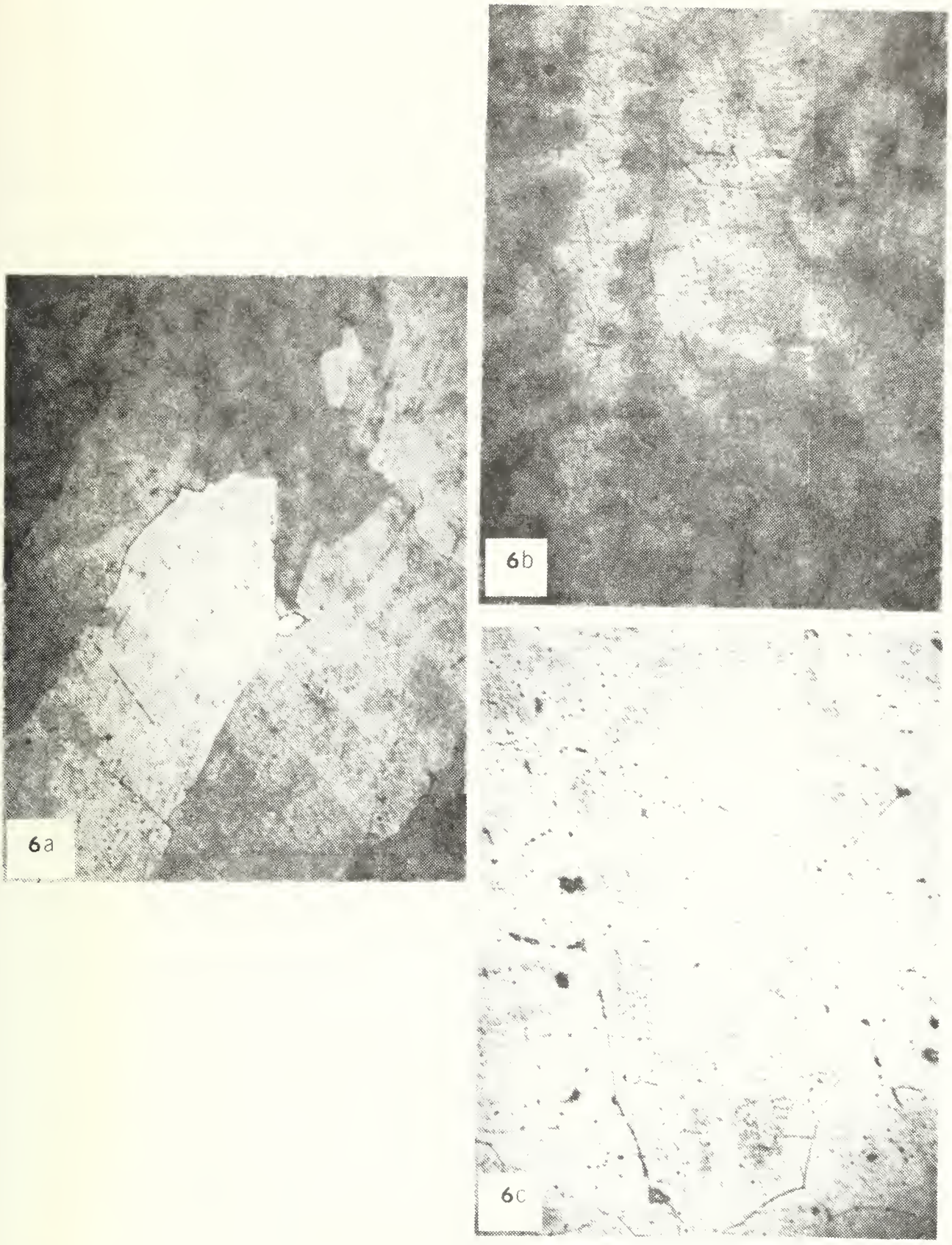

Figure 6. Base-metal microstructures of three aluminum sacrificial anode alloys. (a) Galvalum I, (b) Reynode II, (c) KA-90. Specimens etched with 0.5% hydrofluoric acid. All magnifications 100X.

Metallography courtesy of R. E. Edwards.

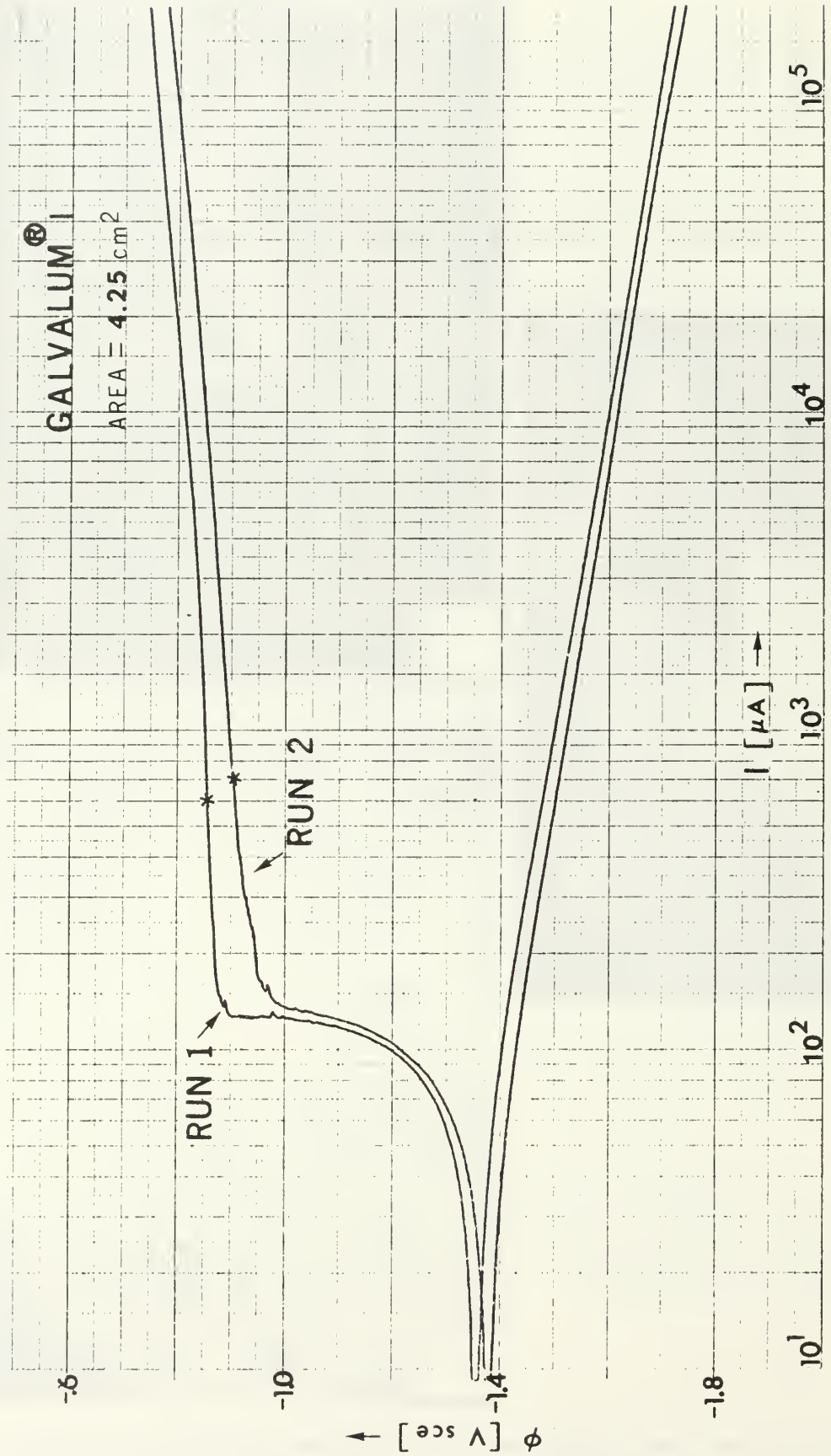
GALVALUM®
AREA = 4.25 cm²
RUN 1
RUN 2
-.6
-1.0
-1.4
-1.8
φ [V sce] →
10¹
10²
10³
10⁴
10⁵
I [μA] →

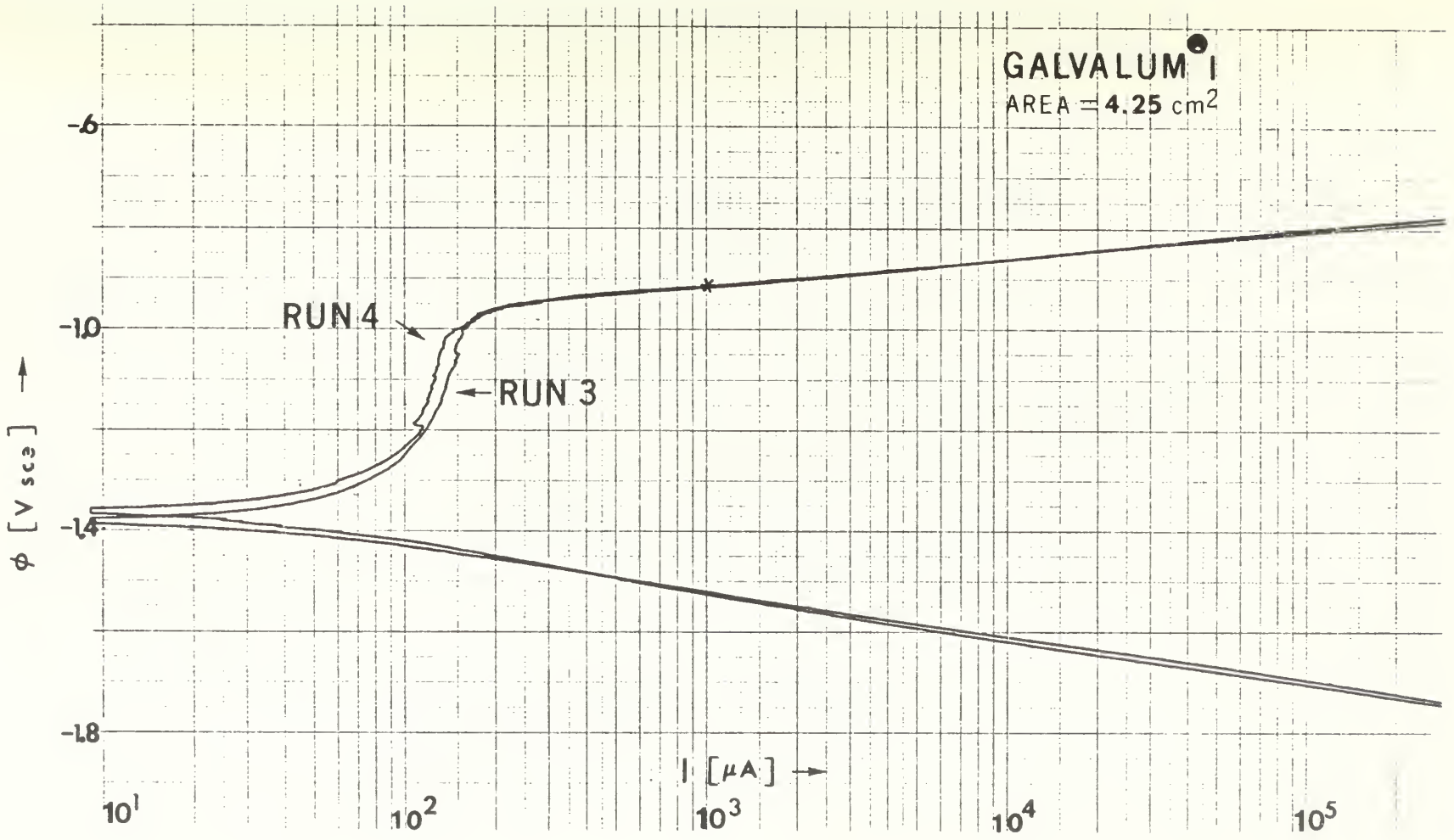

Figure 7 (a): Potentiodynamic polarization curves for Galvalum I in synthetic seawater. Scan direction upward at 1.0 mV/sec. Four separate runs shown, each for a fresh sample and electrolyte.

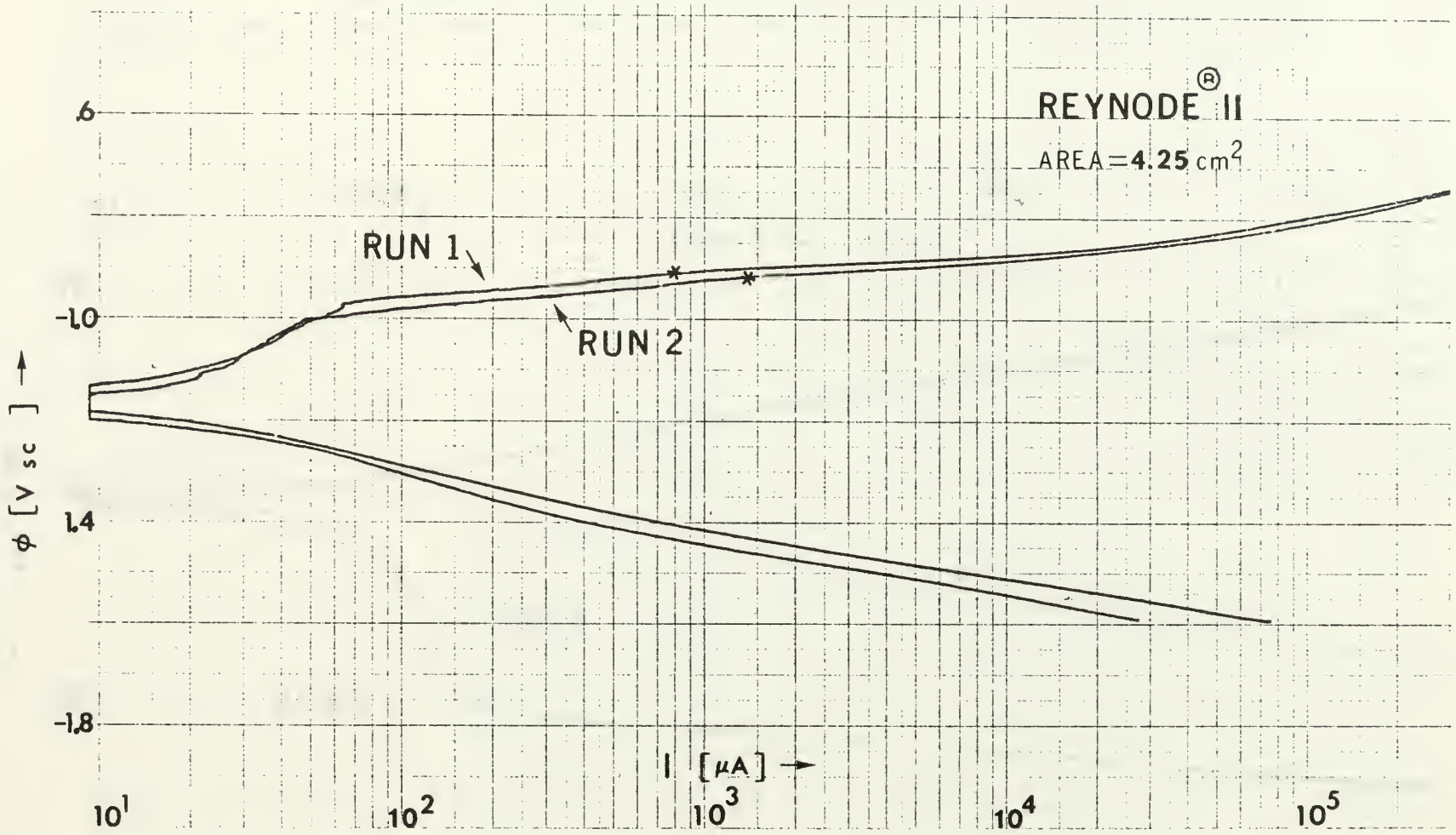
REYNODE® II
AREA = 4.25 cm²
RUN 1
RUN 2
.6
-1.0
1.4
-1.8
φ [V sc] →
I [μA] →
10¹
10²
10³
10⁴
10⁵

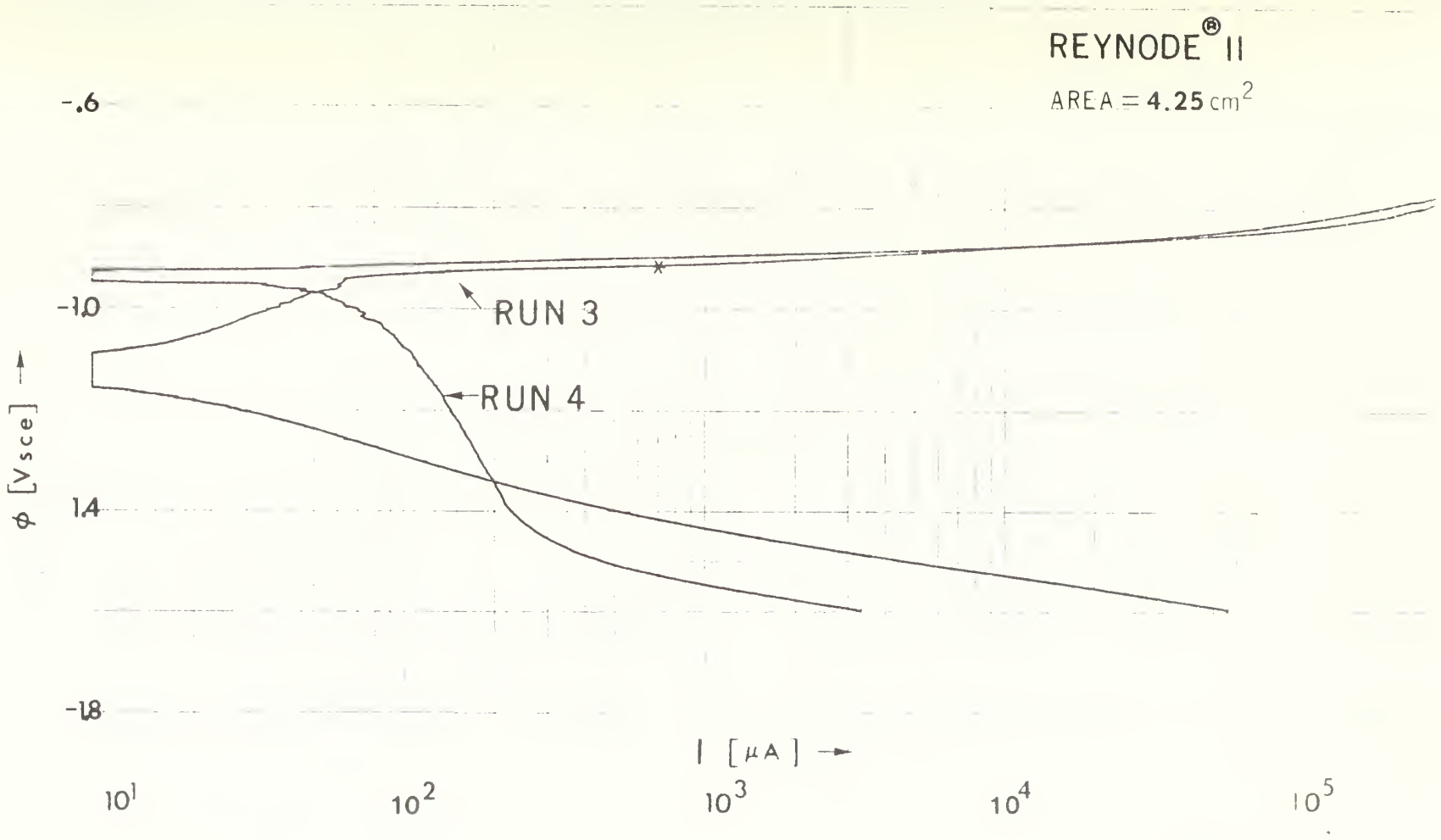

Figure 7 (b): Potentiodynamic polarization curves for Reynode II in synthetic seawater. Scan direction upward at 1.0 mV/sec. Four separate runs shown, each for a fresh sample and electrolyte.

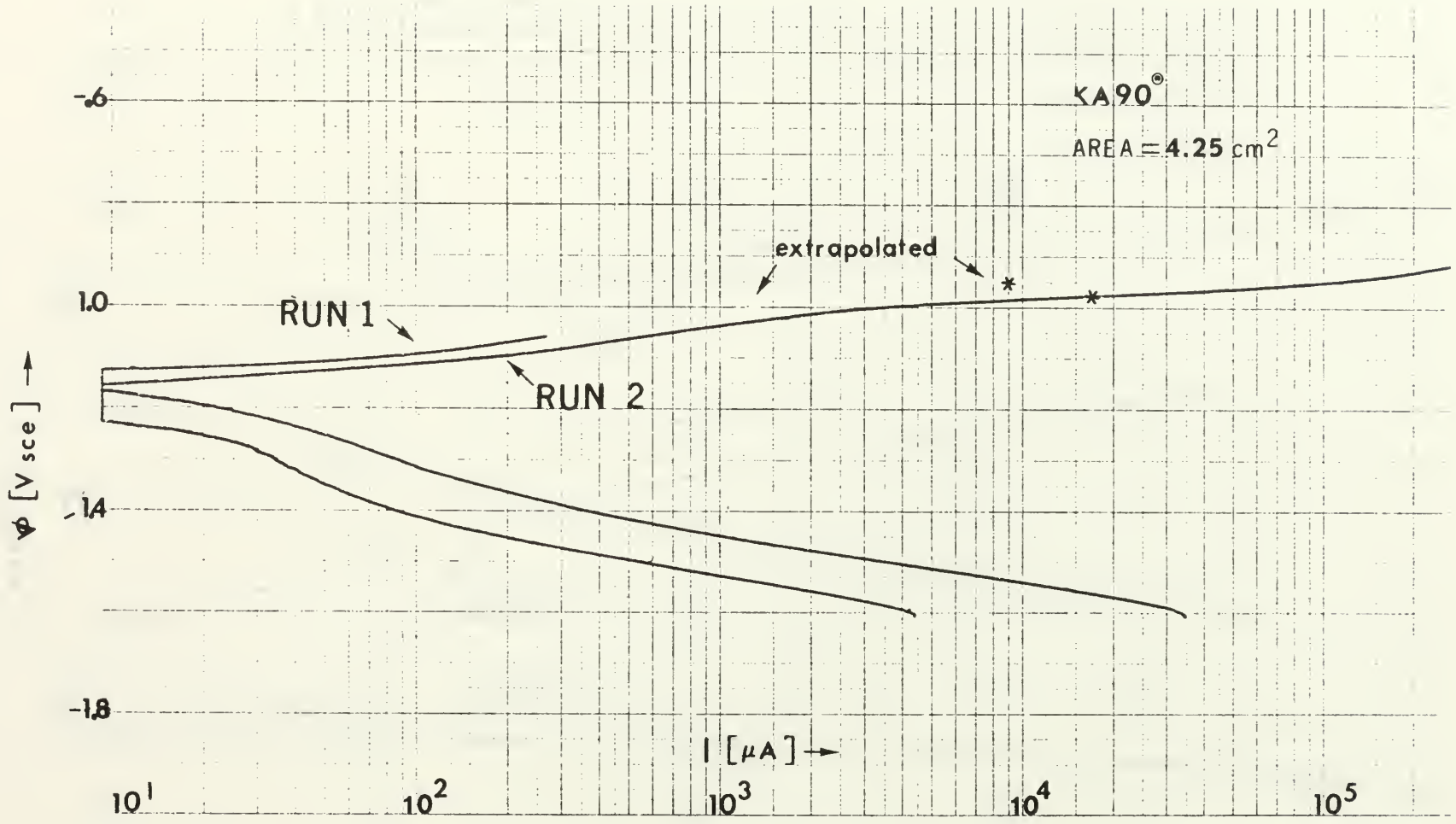
KA 90°
AREA = 4.25 cm²
extrapolated
RUN 1
RUN 2
-.6
1.0
1.4
1.8
φ [V sce] →
I [μA] →
10¹
10²
10³
10⁴
10⁵

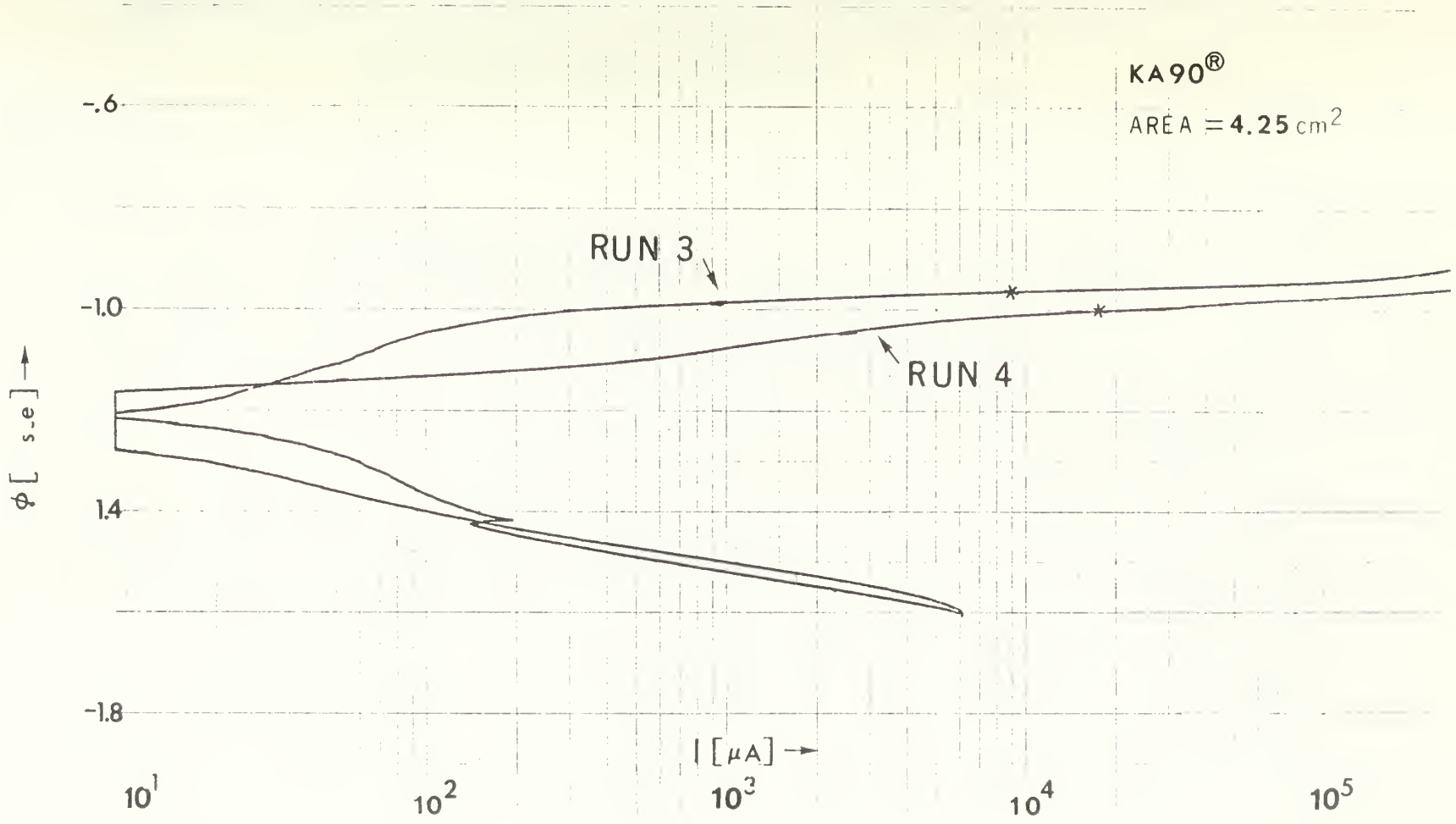

Figure 7 (c): Potentiodynamic polarization curves for KA-90 in synthetic seawater. Scan direction upward at 1.0 mV/sec. Four separate runs shown, each for a fresh sample and electrolyte.

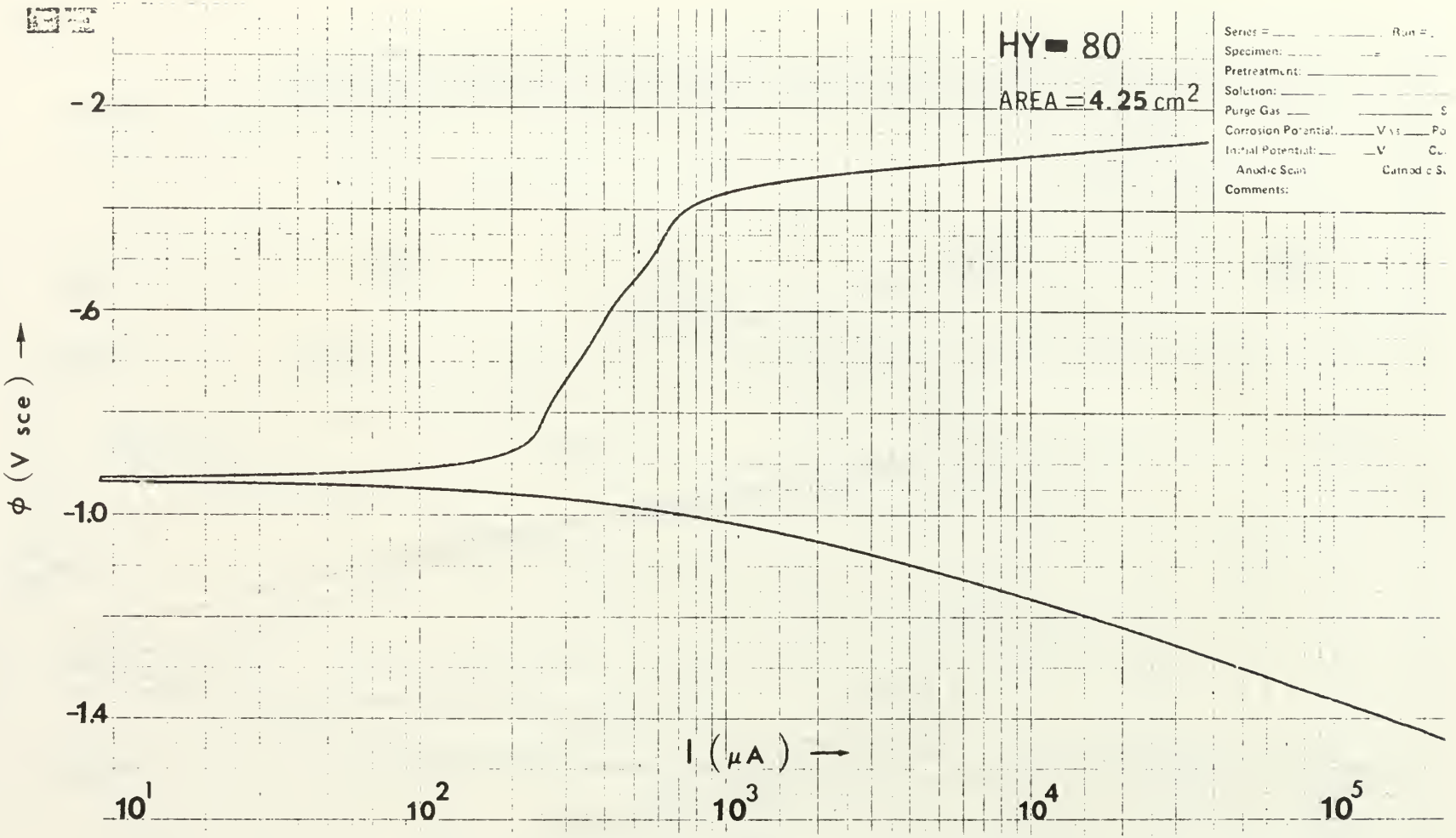

Figure 7 (d): Potentiodynamic polarization curve for HY-80 steel in synthetic seawater. Scan direction upward at 1.0 mV/sec.

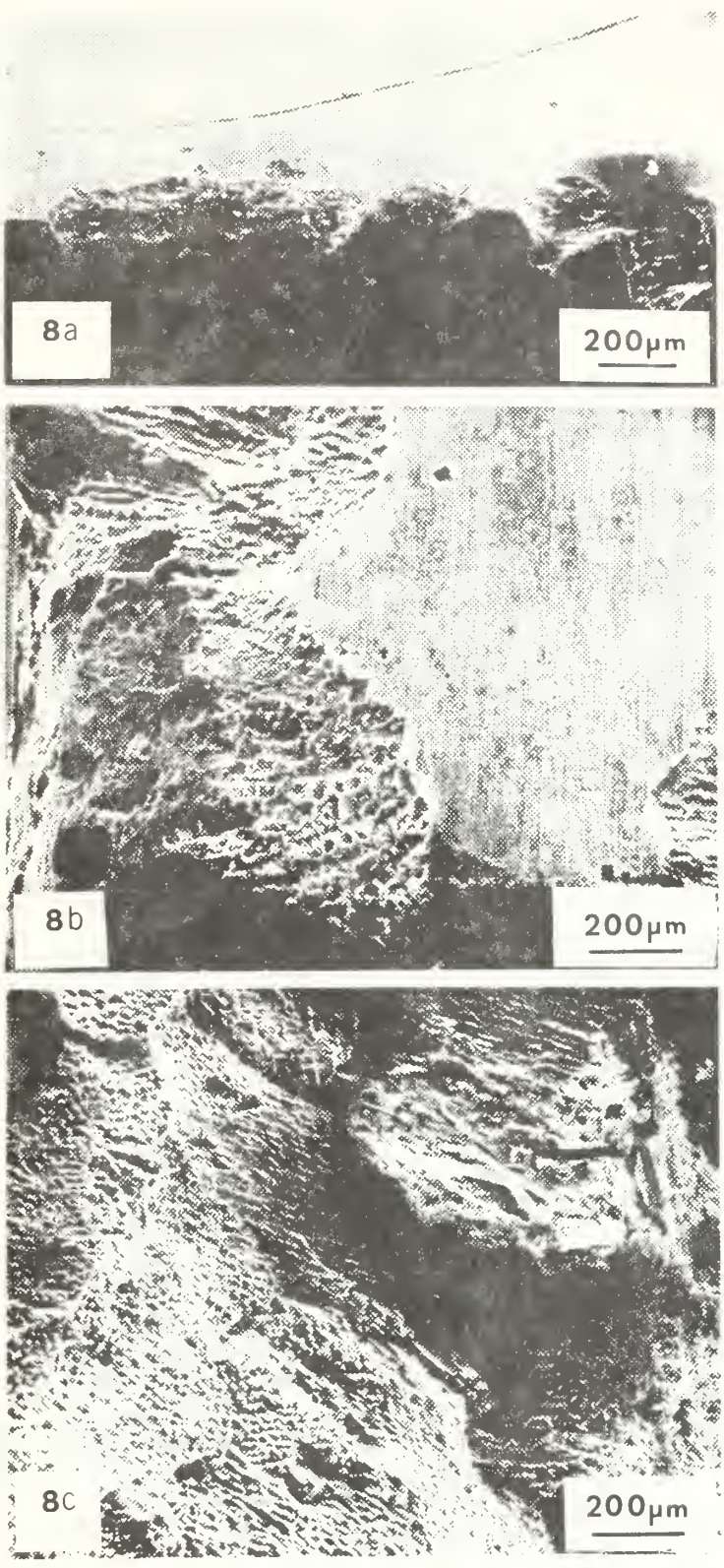

Figure 8: Low-magnification scanning electron micrographs of Galvalum I anode coupons after various times coupled to HY-80 steel (area ratio 1:27) in synthetic seawater. (a) 0.25 hr., 50X corroded area localized on edge of specimen, (b) 4 hrs, 60X, dissolution regions advancing inward from specimen edges, (c) 48 hrs, 60X, further expansion of dissolution region.

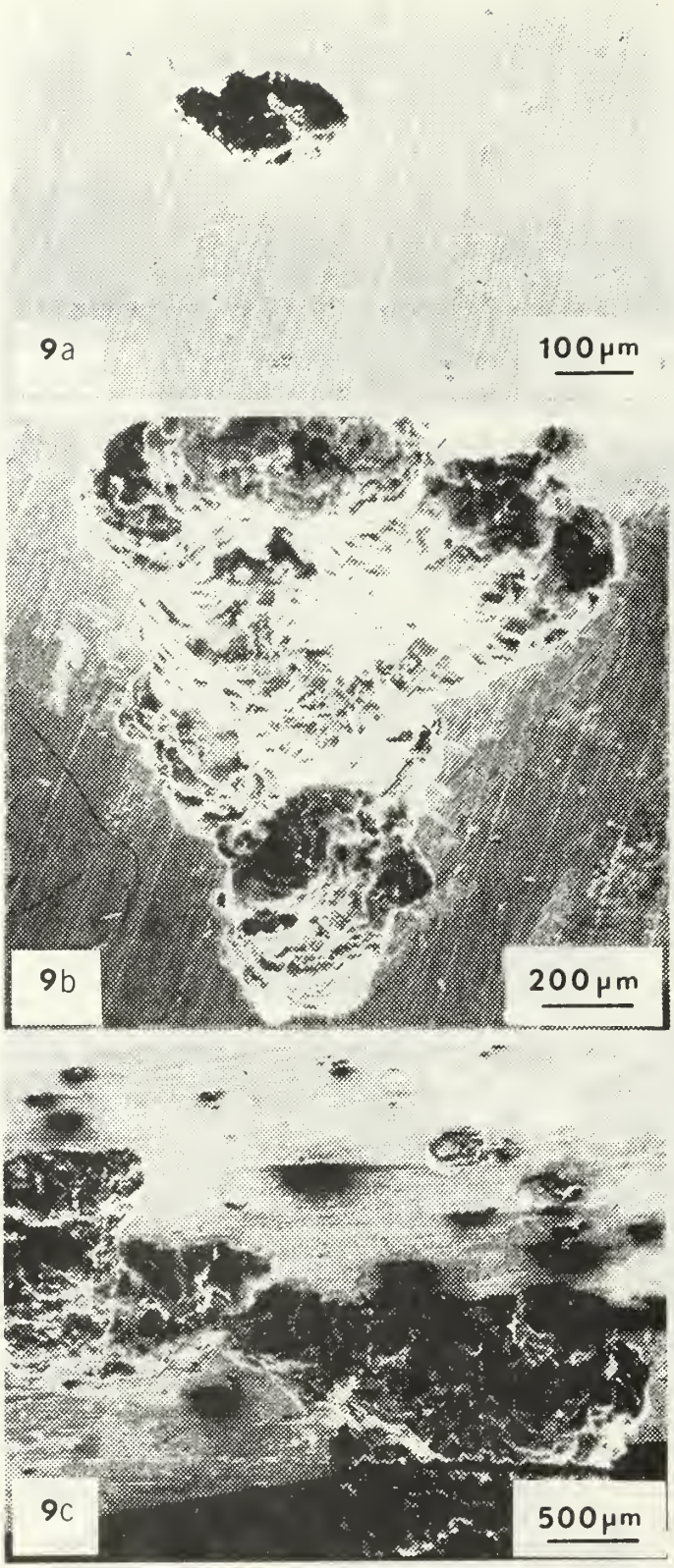

Figure 9: Low-magnification scanning electron micrographs of Reynode II anode coupons after various times coupled to HY-80 steel (area ratio 1:27) in synthetic seawater. (a) 0.25 hr., 100X, local dissolution sites initiated on broad face of specimen, (b) 8 hrs., 60X, expansion of dissolution cavity on broad face of specimen, (c) 24 hrs, 25X, continued growth of dissolution cavity, (d) 48 hrs, 25X, (e) 72 hrs., 25X, the dissolution vavities elongate down the vertical faces of the anodes.


9d
500 µm

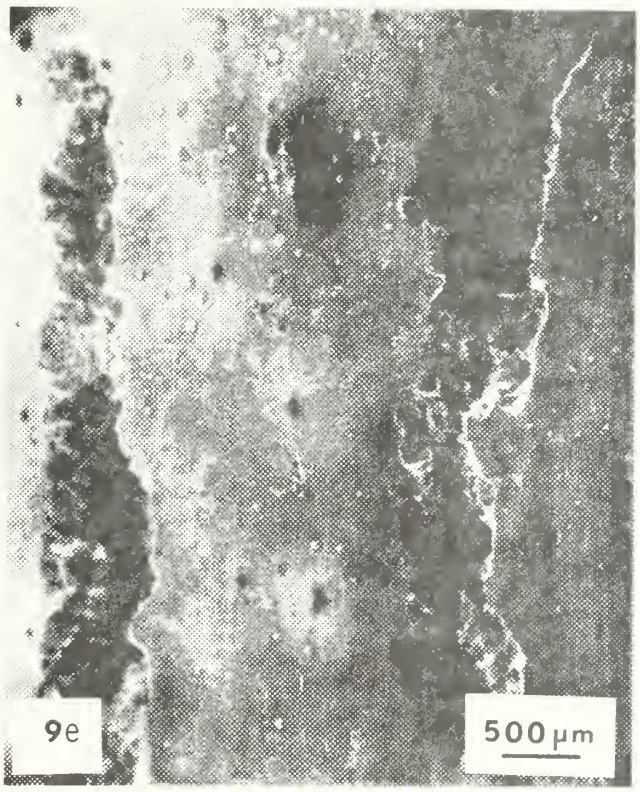
9e
500 µm

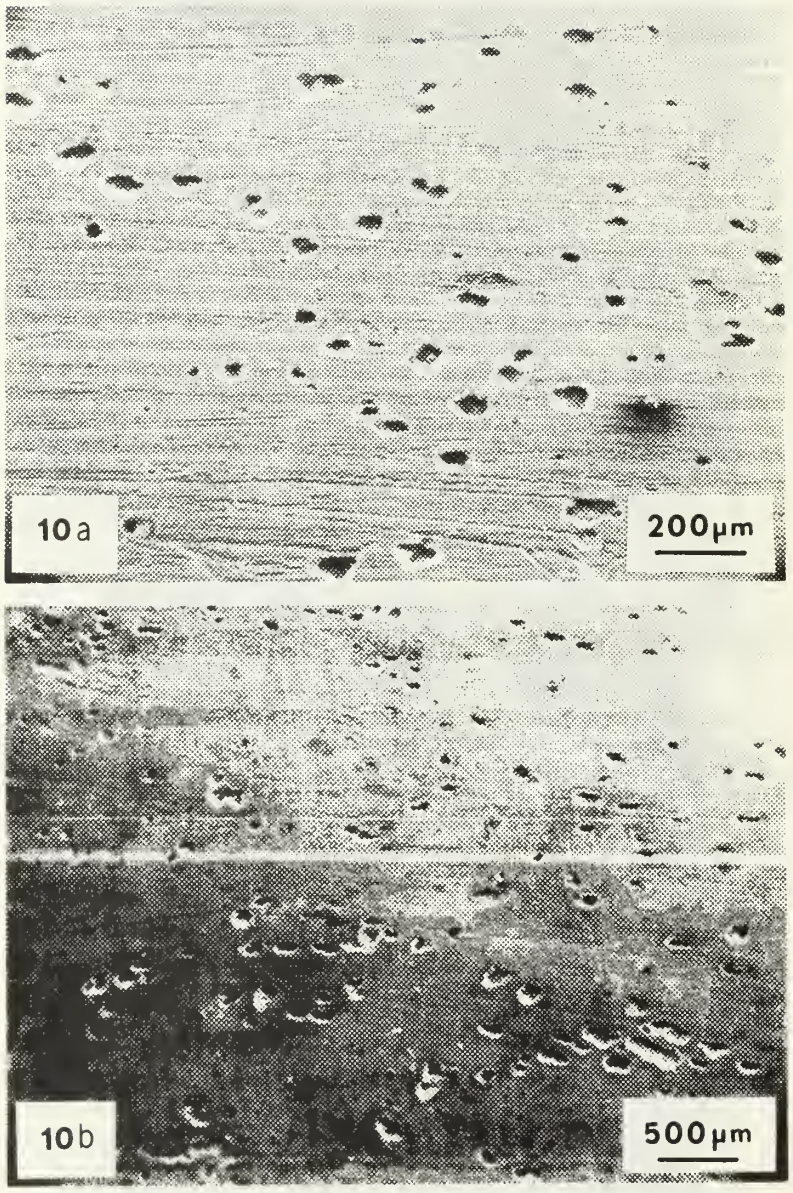

Figure 10: Low-magnification scanning electron micrographs of KA-90 anode coupons after various times coupled to HY-80 steel (area ratio 1:27) in synthetic seawater. (a) 0.5 hrs., 60X, distribution of initial dissolution sites on broad face of specimen, (b) 1.0 hr., 20X, (c) 12 hrs., 20X, (d) 24 hrs., 20X, (e) 48 hrs., 60X, note accumulation of corrosion product near dissolution sites.

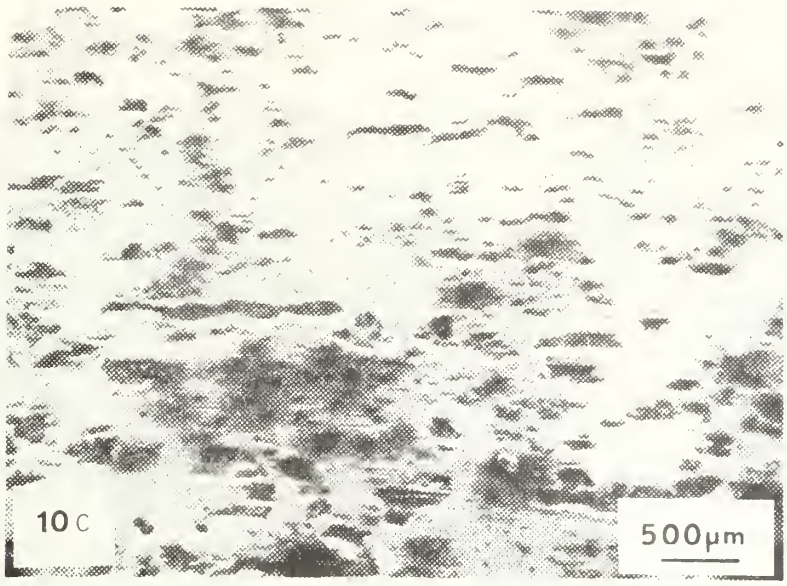
10c
500μm

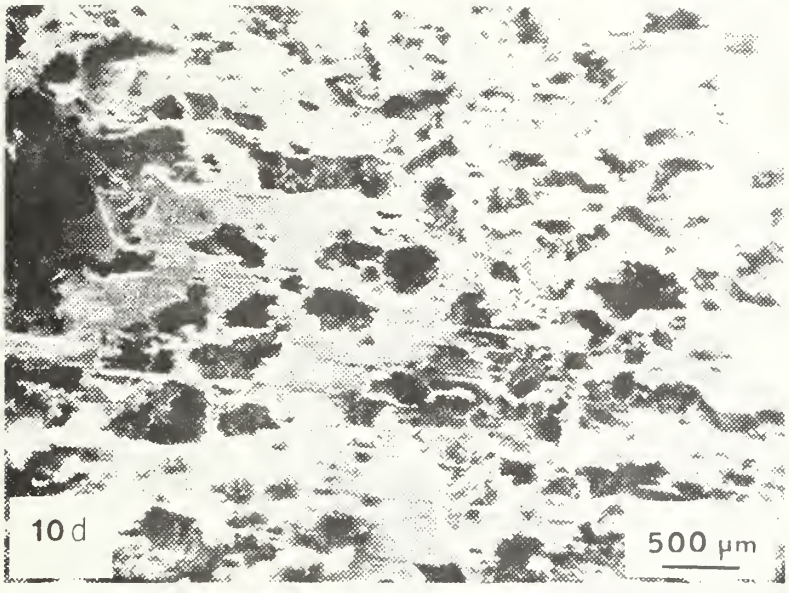
10d
500 μm

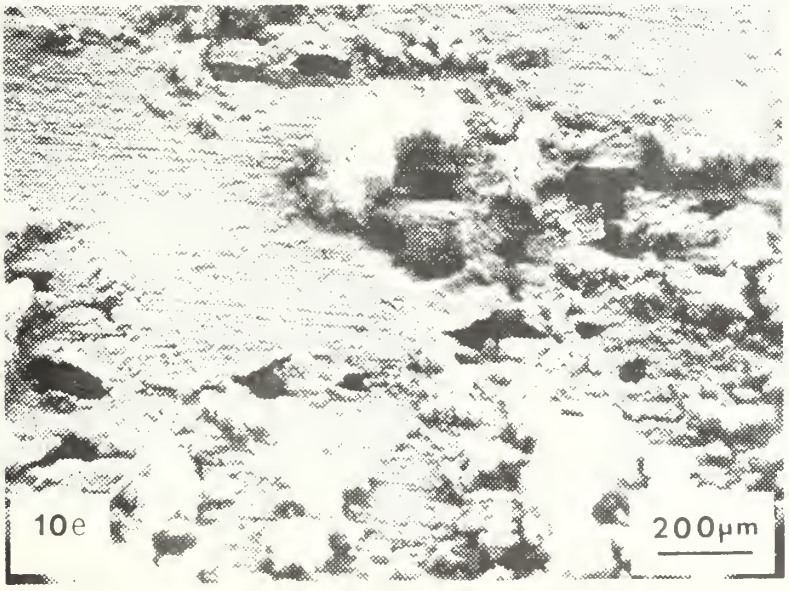
10e
200μm

100 µm
11a
10 µm
11b
20 µm
11c
50 µm
11d

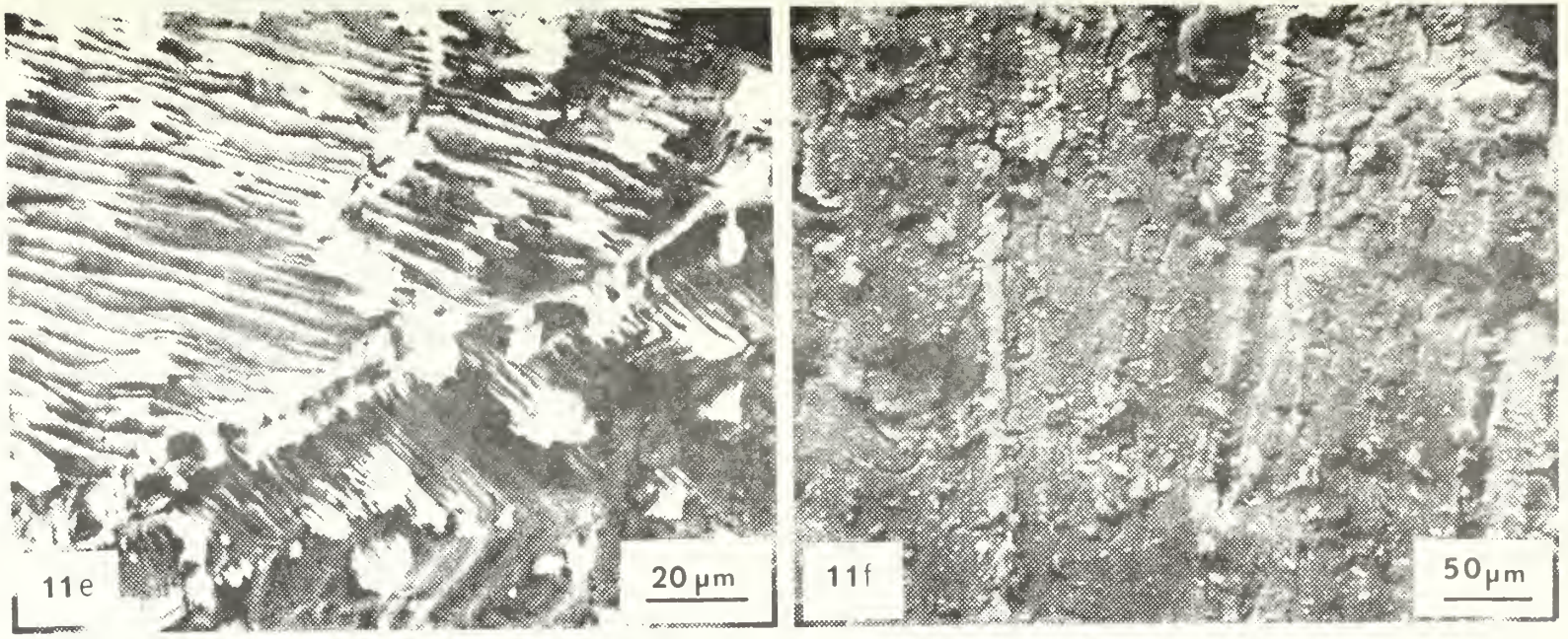

Figure 11: Scanning electron micrographs of dissolution morphology of Galvalum I anodes (a) 1 hour, 120X, regular pattern evident in each base metal grain, (b) 1 hour, 1200X, magnified view of region, showing characteristic "Herringbone" step pattern of dissolution morphology, (c) 1 hour, 600X, note steps on grain at upper right, (d) 2 hrs., 250X, note directionality of dissolution surface pattern in each grain, (e) 2 hrs., 650X, grain boundary evident on dissolution surface, (f) 4 hrs., 2300X, cracked compact film on uncorroded region of anode surface, (g) 24 hrs., 220X, "herringbone" step structure in dissolution region, with an increase in the amount of corrosion product (white clusters): note slight undercutting of general surface film, (h) 24 hrs., 2000X, magnified view of corrosion product clustering on steps of disolution surface, (i) 96 hrs., 230X, (j) 96 hrs., 600X.

50 µm
11g
5 µm
11h
50 µm
11i
20 µm
11j

Figure 11: Scanning electron micrographs of dissolution morphology of Galvalum I anodes (a) 1 hour, 120X, regular pattern evident in each base metal grain, (b) 1 hour, 1200X, magnified view of region, showing characteristic "Herringbone" step pattern of dissolution morphology, (c) 1 hour, 600X, note steps on grain at upper right, (d) 2 hrs., 250X, note directionality of dissolution surface pattern in each grain, (e) 2 hrs., 650X, grain boundary evident on dissolution surface, (f) 4 hrs., 2300X, cracked compact film on uncorroded region of anode surface, (g) 24 hrs., 220X, "herringbone" step structure in dissolution region, with an increase in the amount of corrosion product (white clusters): note slight undercutting of general surface film, (h) 24 hrs., 2000X, magnified view of corrosion product clustering on steps of disolution surface, (i) 96 hrs., 230X, (j) 96 hrs., 600X.

12a
50µm
12b
10µm
12c
10µm
12d
50µm

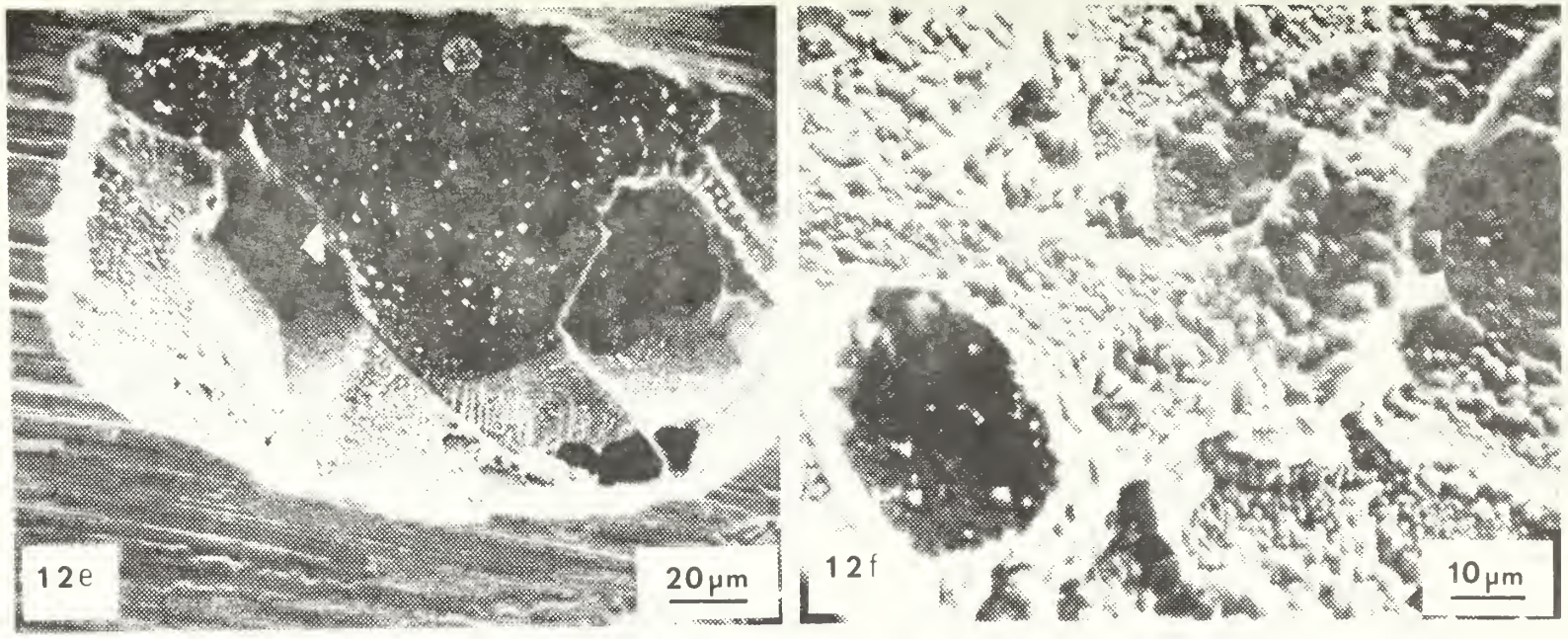

Figure 12: Scanning electron micrographs of dissolution morphology of Reynode II anodes (a) 0.5 hr., 200X, ridges evident along grain boundaries within dissolution region, (b) 0.5 hr., 1000X, magnified view of grain boundary ridge near center, (c) 0.5 hr., 1000X magnified view of grain surface, showing characteristic "peak" morphology, (d) 1 hr., 250X (e) 1 hr., 500X, note distinct definition of grain surface facets (f) 1 hr., 1000X, "peak" morphology evident at high magnification, (g) 2 hrs., 500X, striated morphology evident on some grain surfaces, (h) 2 hrs., 1000X, "peak" morphology (i) 4 hrs., 100X, (j) 4 hrs., 1000X, (k) 8 hrs., 1000X, (l) 24 hrs., 1000X, (m) 72 hrs., 600X, note striated dissolution morphology in some grains, peak morphology in others.

20µm
12g
10µm
12h
100µm
12i
10µm
12j

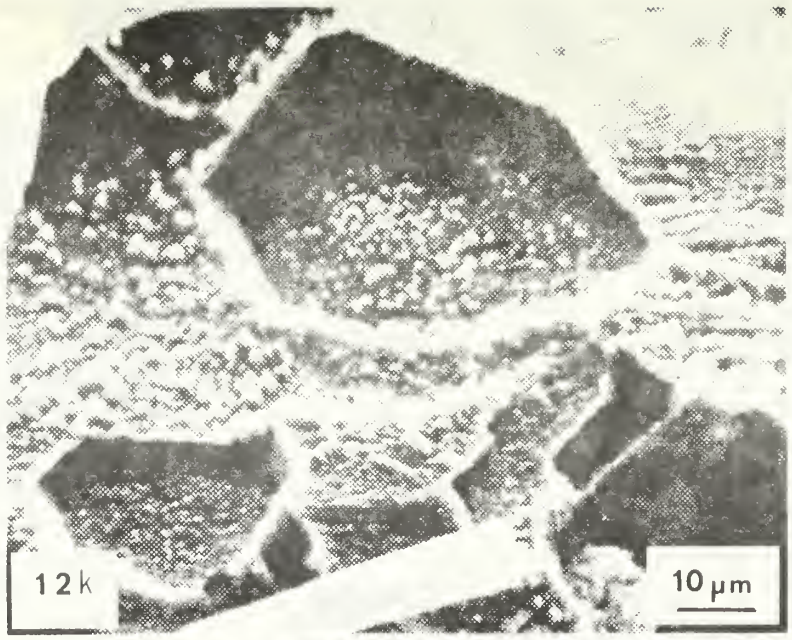
12k
10 µm

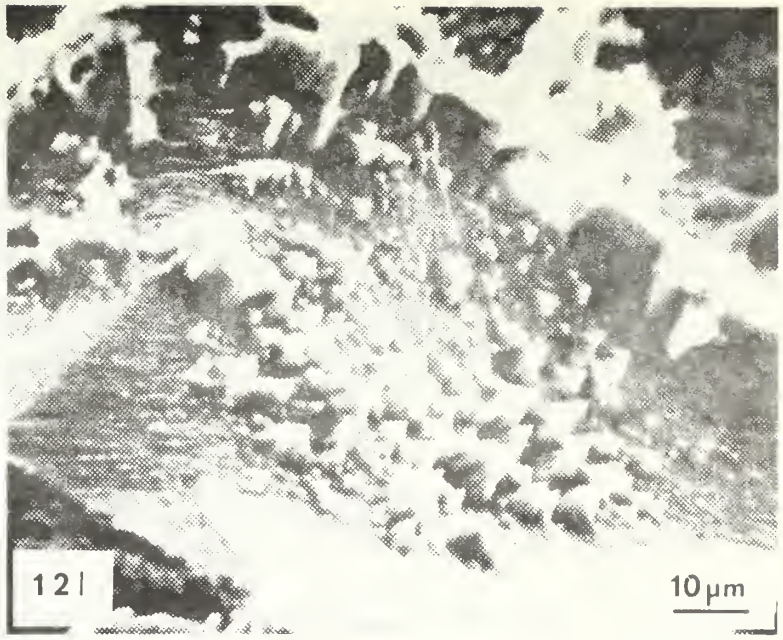
12l
10 µm

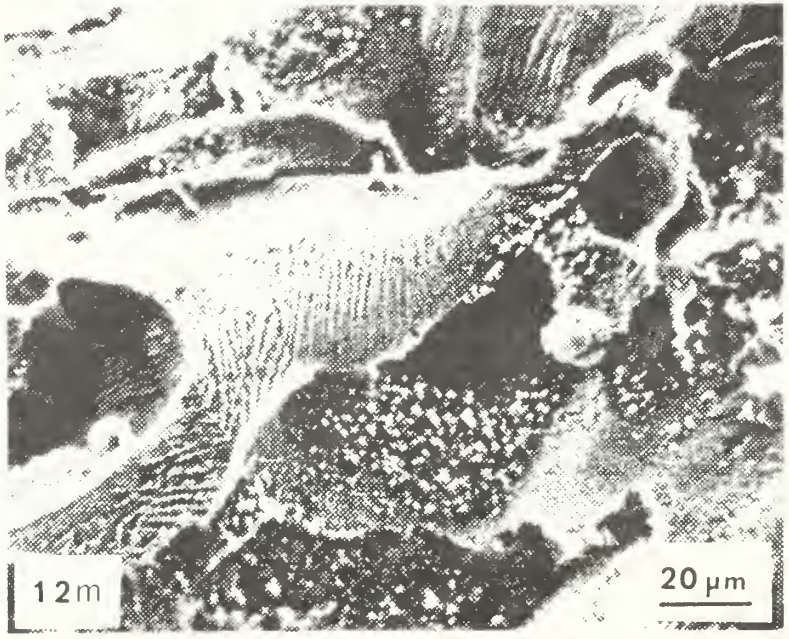
12m
20 µm

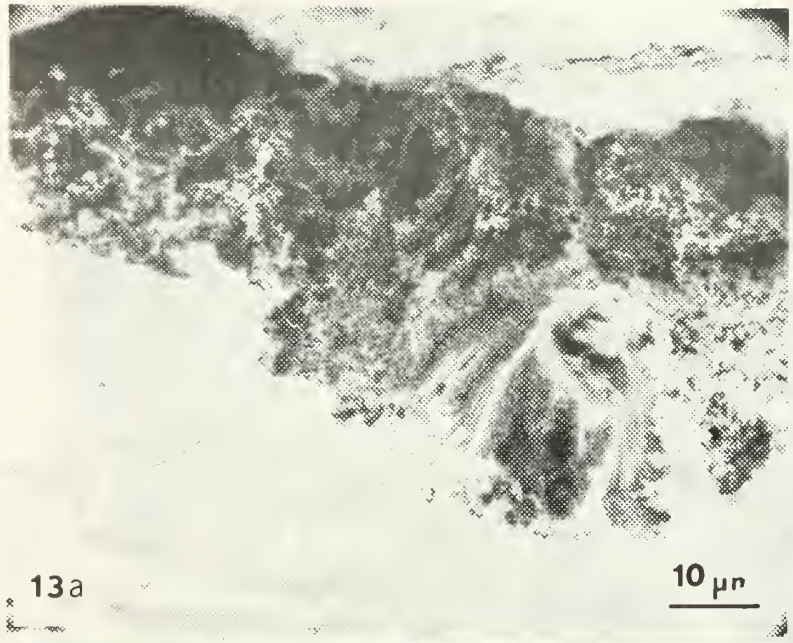
13a
10 µm

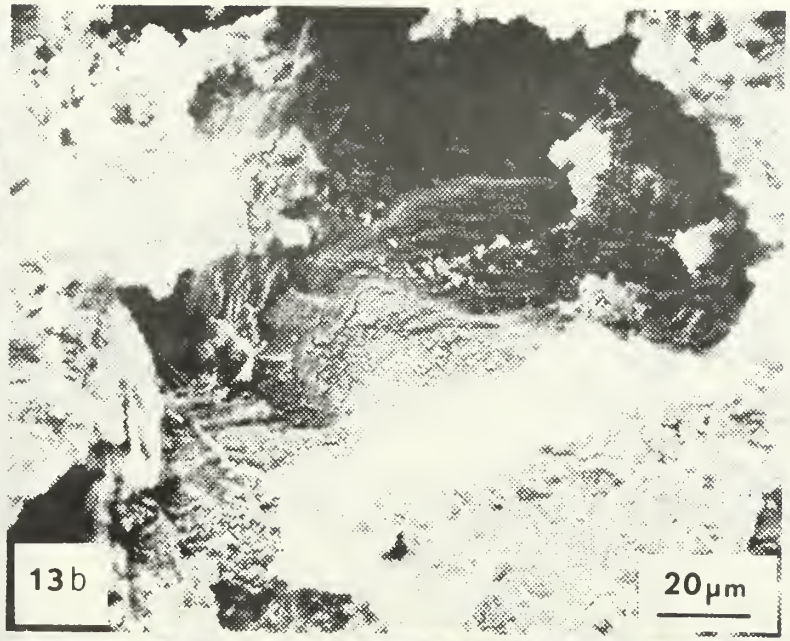
13b
20µm

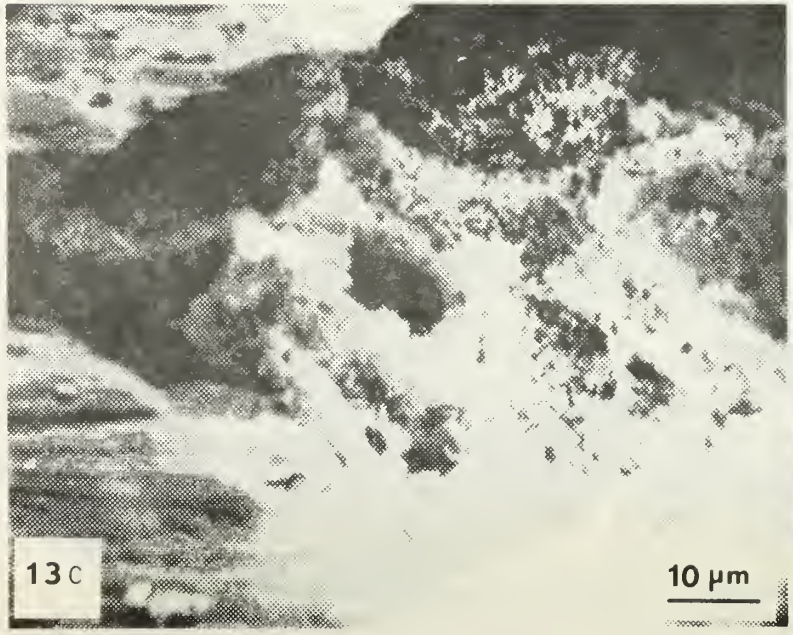
13c
10 µm

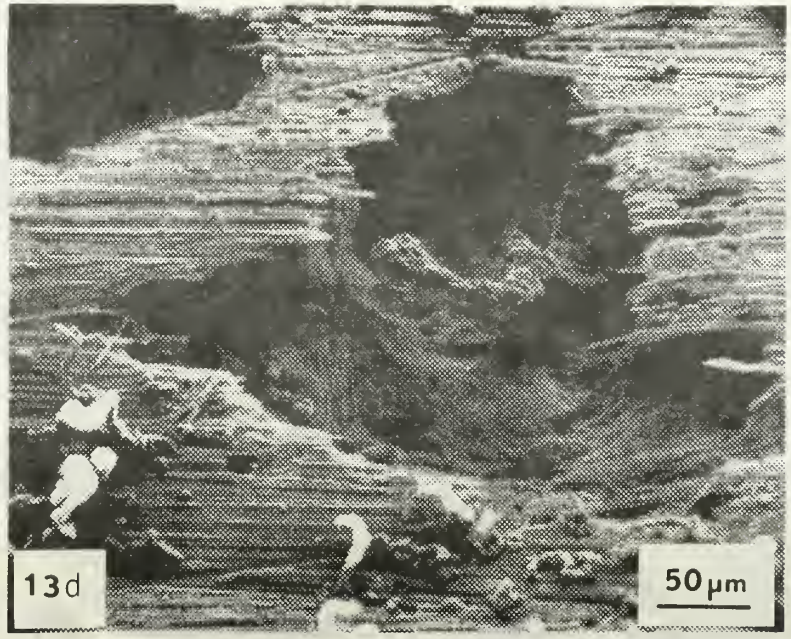
13d
50µm

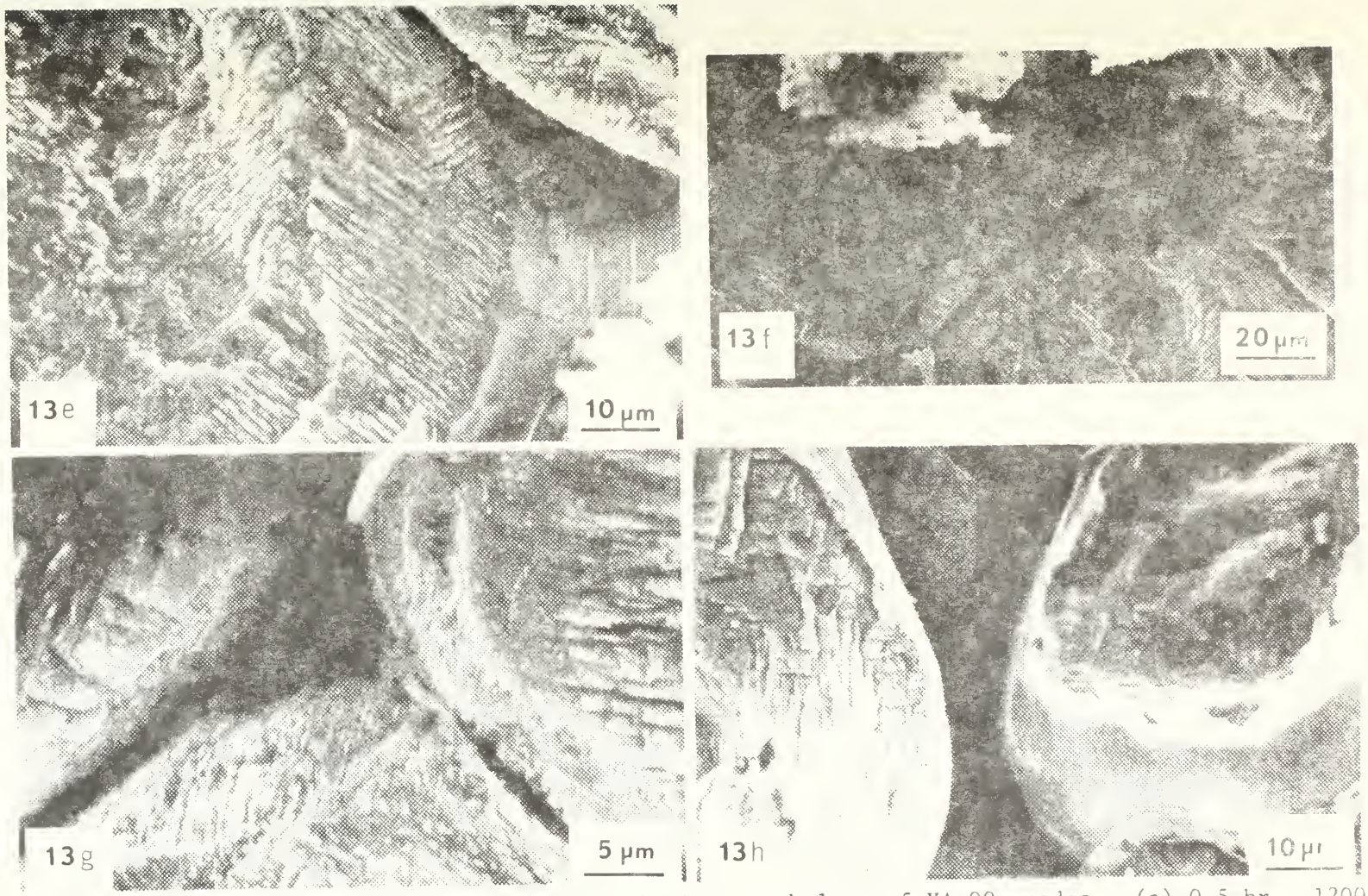

Figure 13: Scanning electron micrographs of dissolution morphology of KA-90 anodes. (a) 0.5 hr., 1200X, dissolution cavity undercutting surface and corrosion product buildup, (b), 1 hr., 600X, surface of dissolution cavity, (c) 2 hr., 1200X, dissolution cavity, (d) 12 hrs., 240X, dissolution cavities; note surface undercutting, (e) 24 hrs., 1200X, note striated step structure on dissolution surface; this structure is only evident when corrosion product falls away from the surface, (f) 24 hrs., 600X, note grain triple point accented by concentrated attack along grain boundaries, (g) 24 hrs., 2400X, close-up of grain triple point, showing grain line penetration, (h) 24 hrs., 1200X encapsulation of grains by smooth corrosion product shells.

INITIAL DISTRIBUTION LIST

		No. Copies
1.	Defense Documentation Center Cameron Station Alexandria, Virginia 22314	2
2.	Library, Code 0142 Naval Postgraduate School Monterey, California 93940	2
3.	Department Chairman, Code 69 Department of Mechanical Engineering Naval Postgraduate School Monterey, California 93940	2
4.	Naval Research Laboratory Washington, D. C. 20390 Code 2627	1
5.	Naval Air Propulsion Test Center Trenton, NJ 08628 Attn: Library	1
6.	Office of Naval Research Department of the Navy (Attn:Code 471) 800 N. Quincy Street Arlington, VA 22217	1
7.	Naval Air Development Center Code 302 Warminster, PA 18974 Attn: Mr. F. S. Williams	1
8.	Naval Construction Battalion Civil Engineering Laboratory Port Hueneme, CA 93043 Attn: Materials Division	1
9.	Office of Naval Research 800 N. Quincy Street Arlington, VA 22217 Attn: Code 102	1
10.	Naval Electronics Lab. Center San Diego, CA 92152 Attn: Electron Materials Sciences Division	1
11.	Naval Missile Center Materials Consultant Code 3312-1 Point Mugu, CA 93041	1

12. Office of Naval Research
800 N. Quincy Street
Arlington, VA 22217
Attn: Code 470 — 1

13. Commanding Officer
Naval Surface Weapons Center
White Oak Laboratory
Silver Spring, MD 20910 — 1

14. David W. Taylor
Naval Ship R & D Center
Materials Department
Annapolis, MD 21402 — 1

15. Commanding Officer
Office of Naval Research
Branch Office
495 Summer Street
Boston, MA 02210 — 1

16. Naval Undersea Center
San Diego, CA 92132
Attn: Library — 1

17. Naval Underwater System Center
Newport, RI 02840
Attn: Library — 1

18. Commanding Officer
Office of Naval Research
Branch Office
536 S. Clark Street
Chicago, IL 60605 — 1

19. Naval Weapons Center
China Lake, CA 93555
Attn: Library — 1

20. Naval Air Systems Command
Washington, D. C. 20360
Attn: Code 52031 — 1

21. Office of Naval Research
San Francisco Area Office
760 Market Street, Rm 447
San Francisco, CA 94102 — 1

22. Naval Air Systems Command
Washington, D. C.
Attn: Code 52032 — 1

23. Naval Air Systems Command
Washington, D. C. 20360
Attn: Code 320 — 1

24. Naval Research Lab. 1
Washington, DC 20390
Attn: Code 6000

25. Naval Sea System Command 1
Washington, DC 20362
Attn: Code 035

26. NASA Headquarters 1
Washington, D. C.
Attn: Code RRM

27. Naval Research Lab. 1
Washington, DC 20390
Attn: Code 6100

28. Naval Facilities 1
Engineering Command
Alexandria, VA 22331
Attn: Code 03

29. NASA 1
Lewis Research Center
20111 Brookpark Road
Cleveland, Ohio 44135
Attn: Library

30. Naval Research Lab. 1
Washington, D.C. 20390
Attn: Code 6300

31. Scientific Advisor 1
Commandant of the Marine Corps
Washington, D. C. 20380
Code AX

32. National Bureau of Standards 1
Washington, DC 20234
Attn: Metallurgy Division
Inorganic Mat. Div.

33. Dr. Wm. R. Prindle 1
National Academy of Sciences
National Research Council
2101 Constitution Ave.
Washington, DC20418

34. Dr. R. P. Wei, Lehigh Univ. 1
Inst. for Fracture &
Solid Mechanics
Bethlehem, PA 18015

35. Prof. H. G. F. Wilsdorf 1
Univ. of Virginia
Dept. of Mat. Science
Charlottesville, VA 22903

36. Defense Metals and Ceramics Info Center
Battelle Mem. Institute
505 King Ave.
Columbus, Ohio 43201 — 1

37. Naval Ship Engr. Center
CTR BG #2 Code 6101
3700 E-W Highway
Prince George Plaza
Hyattsville, MD 20782 — 1

38. Director, Ordnance Research Lab.
P.O. Box 30
State College, PA 16801 — 1

39. Army Research Office
Box CM, Duke Station
Durham, NC 27706
Attn: Metallurgy & Cer. Div. — 1

40. Army Materials and Mechanics Research Center
Watertown, MA 02172
Attn: (AMXMR-P) — 1

41. Dir. Applied Physics Lab.
University of Washington
1013 NE 40th Street
Seattle, WA 98105 — 1

42. Metals and Ceramics Div.
Oak Ridge Nat'l Lab.
P.O. Box X
Oak Ridge, TN 37380 — 1

43. AF/Ofc. of Scientific Research
Bldg. 410 Bolling AF Base
Washington, D. C. 20332
Attn: Chem. Sci. Directorate
Electronics & S. S. Sci. Director — 1

44. Los Alamos Scientific Lab
P.O. Box 1663
Los Alamos, NM 87544
Attn: Report Librarian — 1

45. AF Materials Lab. (LA)
Wright-Patterson AFBase
Dayton, Ohio 45433 — 1

46. Argonne National Lab.
Metallurgy Division
P.O. Box 229
Lemont, IL 60439 — 1

47. Dr. J. A. S. Green — 1
Martin Marietta Corp.
1450 S. Rolling Road
Baltimore, MD 21227

48. Dr. T. R. Beck — ;
Electrochemical Tech. Corp.
10035 31st Ave. NE
Seattle, WA 98125

49. Prof. R. H. Heidersbach — 1
University of Rhode Island
Department of Ocean Engr.
Kingston, RI 02881

50. Professor I. M. Bernstein — ;
Carnegie-Mellon Univ.
Schenley Park
Pittsburgh, PA 15213

51. Professor H. K. Birnbaum — 1
Univ. of Illinois
Dept. of Metallurgy
Urbana, IL 61801

52. Prof. J. P. Hirth — 1
Ohio State University
Metallurgical Engineering
Columbus, OH 43210

53. Prof. H. Herman — 1
State Univ. of New York
Materials Science Div.
Stony Brook, NY 11794

54. Dr. Otto Buck — 1
Rockwell International
1049 Camino Dos Rios
P.O. Box 1085
Thousand Oaks, CA 91360

55. Dr. D. W. Hoeppner — 1
University of Missouri
College of Engineering
Columbia, MO 65201

56. Prof. H. W. Pickering — 1
Pennsylvania State Univ.
Dept. of Mat. Sciences
University Park, PA 16802

57. Dr. David L. Davidson — 1
Southwest Research Inst.
8500 Culebra Road
P.O. Drawer 28510
San Antonio, TX 78284

58. Dr. E. W. Johnson — 1
Westinghouse Electric Corp.
Research and Development Center
1310 Beulah Road
Pittsburgh, PA 15235

59. Dr. F. Mansfeld — 1
Rockwell
1049 Camino Dos Rios
P.O. Box 1085
Thousand Oaks, CA 91360

60. Dr. D. J. Duquette — 1
Dept. of Metallurgical Engr.
Rensselaer Polytechnic Inst.
Troy, NY 12181

61. Prof. R. T. Foley — 1
The American University
Dept. of Chemistry
Washington, DC 20016

62. Prof. A. E. Miller — 1
University of Notre Dame
College of Engineering
Notre Dame, IN 46556

63. Mr. G. A. Gehring — 1
Ocean City Research Corp.
Tennessee Ave. & Beach Thorofare
Ocean City, NJ 08226

64. Prof. R. W. Staehle — 1
Ohio State University
Dept. of Metallurgical Engr.
Columbus, OH 43210

65. Dr. Barry C. Syrett — 1
Stanford Research Institute
333 Ravenswood Avenue
Menlo Park, CA 94025

66. Brookhaven Nat'l Laboratory — 1
Technical Info. Div.
Upton, LI
New York 11973
Attn: Research Library

67. Library — 1
Building 50 Rm 134
Lawrence Radiation Laboratory
Berkeley, CA 94550

68. Prof. Jeff Perkins — 30
Naval Postgraduate School
Code (69Ps)
Monterey, CA 93940